

1

# Snow Interception Relationships with 2 Meteorology and Canopy Structure in a 3 Subalpine Forest

4

5 **Authors:**

6 A. Cebulski<sup>1</sup> (ORCID ID - 0000-0001-7910-5056)

7 J.W. Pomeroy<sup>1</sup> (ORCID ID - 0000-0002-4782-7457)

8 <sup>1</sup>Centre for Hydrology, University of Saskatchewan, Canmore, Canada

9 **Corresponding Author:** A. Cebulski, alexcebulski@gmail.com

10 **Abstract:** Snow accumulation models differ in how snow interception and ablation processes  
11 are represented and thus their application to diverse climates and forest types is uncertain.  
12 Existing parameterizations of initial snow interception before unloading include inherently  
13 coupled canopy snow accumulation and ablation processes. This leads to difficulty in di-  
14 agnosing processes and adding possible errors to simulations when incorporated as canopy  
15 interception routines in models that already account for canopy snow ablation. This study  
16 evaluates the theory underpinning parameterizations of initial snow interception using high-  
17 temporal resolution and fine-scale measurements of throughfall for events with minimal snow  
18 ablation and redistribution in both the canopy and on the ground. The relationship between  
19 these throughfall measurements, event meteorology, and a novel lidar-based canopy strucutre  
20 measurement are assessed in two subalpine forest plots in the Canadian Rockies. Contrary  
21 to existing theories, no association of canopy snow load or air temperature with interception

efficiency was observed. Instead, canopy structure emerged as the primary factor governing snow accumulation. A wind-driven snowfall event demonstrated that non-vertical hydrometeor trajectories can significantly increase snow-leaf contact area, thereby enhancing initial interception before ablation. Prediction of interception efficiency for this event improved dramatically when adjusted for hydrometeor trajectory angle based on a wind speed at one-third of the canopy height. Snow-leaf contact area showed a high sensitivity to wind speed, increasing by up to 95% with a  $1 \text{ m s}^{-1}$  wind speed. The study proposes a new parameterization that calculates throughfall, independent of processes that ablate snow from the canopy, as a function of snow-leaf contact area adjusted for hydrometeor trajectory angle. This new parameterization successfully estimated subcanopy snow accumulation for a snowfall event at two forest plots measured using lidar and snow surveys. By separating canopy snow ablation from snow interception processes, this new model offers potentially improved prediction of subcanopy snow accumulation when combined with canopy snow ablation parameterizations.

**Keywords:** snow interception, throughfall, ablation, forest, snowpack, lidar, process-based modelling

## 1 Introduction

Over half of North America's snow-covered zone is covered by forests (Kim et al., 2017), significantly impacting the accumulation and redistribution of snowpacks and subsequent snowmelt runoff. Essery et al. (2003) estimated that 25–45% of annual snowfall may be lost to the atmosphere due to sublimation of snow intercepted in forest canopies globally. Snow intercepted in the canopy can sublimate and melt at much higher rates than the subcanopy snowpack (Floyd, 2012; Lundberg & Hallidin, 1994; Pomeroy et al., 1998), reducing the amount of snow available for runoff. Vegetation structure is one of the primary factors controlling the partitioning of snowfall into throughfall and interception, and thus governs the quantity of snow subject to sublimation from the canopy (Hedstrom & Pomeroy, 1998; Storck et al., 2002). However, forest thinning efforts aimed at limiting sublimation losses to increase snowmelt runoff do not

48 always lead to a corresponding increase in spring streamflow (Golding & Swanson, 1978; Har-  
49 pold et al., 2020; Pomeroy et al., 2012; Troendle, 1983). This may be due to increased ablation  
50 rates when forest cover is reduced, desynchronization of snowmelt, and sub-surface hydrology  
51 interactions (Ellis et al., 2013; Musselman et al., 2015; Pomeroy et al., 1997; Safa et al., 2021;  
52 Varhola et al., 2010). Due to the significant impact of forest cover on snow accumulation and  
53 ablation, and sparse or absent monitoring networks for subcanopy snow accumulation (Rittger  
54 et al., 2020; Vionnet et al., 2021), land management, ecological conservation and water re-  
55 source decisions rely on robust models of snow redistribution to estimate past, current and  
56 future subcanopy snowpacks.

57 Hedstrom & Pomeroy (1998), working in the cold continental boreal forest, proposed that ini-  
58 tial snow interception efficiency was controlled by the maximum canopy load which itself was  
59 a function of leaf area index and new snow density. Unloading was found to be an exponential  
60 function of time and observed only days or weeks after the interception event. Storck et al.  
61 (2002), working in temperate coastal forests, emphasized the role of leaf area index and air tem-  
62 perature in controlling the maximum canopy snow load. The opposing relationship between air  
63 temperature and maximum canopy snow load in the Hedstrom & Pomeroy (1998) and Storck  
64 et al. (2002) parameterizations is shown in Clark et al. (2015) Figure 4. Gelfan et al. (2004)  
65 demonstrated accurate subcanopy snowpack simulations at study sites in Russia by treating  
66 the Hedstrom & Pomeroy (1998) and Storck et al. (2002) parameterizations separately while  
67 using a step-based function to choose either parameterization based on temperature. A similar  
68 parameterization in the Cold Regions Hydrological Model (Pomeroy et al., 2022) has shown  
69 strong performance at sites across Canada, northern United States, Switzerland, and Spain.  
70 However, overestimation of subcanopy snow accumulation was reported by Lundquist et al.  
71 (2021) and Lumbrazo et al. (2022) when combining the Hedstrom & Pomeroy (1998) routine  
72 with ablation parameterizations from different studies (e.g., Roesch et al., 2001). The coupling  
73 of ablation processes within existing snow interception models (Hedstrom & Pomeroy, 1998;  
74 Storck et al., 2002) may contribute to overestimates of throughfall, canopy snow unloading,  
75 and canopy snow melt when combined with other canopy snow ablation parameterizations

76 (Cebulski & Pomeroy, 2024). Additional observations of snow interception that exclude abla-  
77 tion processes could help determine the applicability of the interception theories proposed by  
78 Hedstrom & Pomeroy (1998) and Storck et al. (2002). Hedstrom & Pomeroy's (1998) theory  
79 also suggests that moderate wind speeds, which can result in more horizontal hydrometeor tra-  
80 jectories and increase the snow-leaf contact area and interception efficiency at the plot scale.  
81 This association has also been shown in rainfall interception studies to decrease throughfall  
82 of rain (Herwitz & Slye, 1995; Van Stan et al., 2011). Despite this importance for rainfall,  
83 the relationship proposed by Hedstrom & Pomeroy (1998), has typically not been included in  
84 snow accumulation models (Clark et al., 2020; Mahat & Tarboton, 2014) as empirical testing  
85 of this relationship is lacking.

86 The objective of this paper is to evaluate the theories underlying existing snow interception  
87 models using high spatial and temporal resolution measurements of subcanopy snow accumu-  
88 lation for events with minimal canopy snow ablation. These new observations are investigated  
89 to address the following research questions:

- 90 1. Are the existing theories regarding the relationships between meteorology and forest  
91 structure and snow interception supported by in-situ observations?
- 92 2. Is snow interception influenced by non-vertical hydrometeor trajectory angles over a  
93 wind-driven snowfall event?
- 94 3. To what extent can these findings inform the development of a new parameterization for  
95 snow interception?

## 96 **2 Theory**

### 97 **2.1 Snow interception**

98 The canopy snow load,  $L$  ( $\text{kg m}^{-2}$ ) can be estimated from the mass balance:

$$\frac{dL}{dt} = q_{sf} + q_{ros} - q_{tf} - q_{unld} - q_{drip} - q_{wind}^{veg} - q_{sub}^{veg} \quad (1)$$

where  $q_{sf}$  is the snowfall rate ( $\text{kg m}^{-2} \text{s}^{-1}$ ),  $q_{ros}$  ( $\text{kg m}^{-2} \text{s}^{-1}$ ) is the rate of rainfall falling on snow intercepted in the canopy,  $q_{tf}$  ( $\text{kg m}^{-2} \text{s}^{-1}$ ) is the throughfall rate ( $\text{kg m}^{-2} \text{s}^{-1}$ ),  $q_{unld}$  is the canopy snow unloading rate ( $\text{kg m}^{-2} \text{s}^{-1}$ ),  $q_{drip}$  is the canopy snow drip rate due to canopy snowmelt ( $\text{kg m}^{-2} \text{s}^{-1}$ ),  $q_{wind}^{veg}$  is the wind transport rate in or out of the control volume ( $\text{kg m}^{-2} \text{s}^{-1}$ ), and  $q_{sub}^{veg}$  is the intercepted snow sublimation rate ( $\text{kg m}^{-2} \text{s}^{-1}$ ). Figure 1 in Cebulski & Pomeroy (2024) presents a visual representation of this mass balance.

During periods with low air temperatures and low wind speeds,  $q_{unld}$ ,  $q_{drip}$ ,  $q_{wind}^{veg}$ , and  $q_{sub}^{veg}$  can be assumed negligible. Interception efficiency,  $\frac{I}{P}$  (-), which is the fraction of snowfall intercepted over  $\Delta t$  before ablation, can then be calculated during these periods as:

$$\frac{I}{P} = \frac{\Delta L}{\overline{q}_{sf}\Delta t} \quad (2)$$

and throughfall,  $q_{tf}$  can be calculated as:

$$q_{tf} = \left(1 - \frac{I}{P}\right) \cdot q_{sf} \quad (3)$$

## 2.2 Hydrometeor trajectory angle

The trajectory angle,  $\theta_h$  of a hydrometeor as the departure in degrees ( $^\circ$ ) from a vertical plane, is shown in Herwitz & Slye (1995) to be calculated as:

$$\theta_h = \arctan \left( \frac{x_h(u_z)}{v_h(D_h)} \right) * \frac{180}{\pi} \quad (4)$$

where  $v_h(D_h)$  is the terminal fall velocity of the hydrometeor ( $\text{m s}^{-1}$ ), which is a function of the hydrometeor diameter,  $D_h$  and  $x_h(u_z)$  is the horizontal velocity of the hydrometeor ( $\text{m}$

<sub>114</sub>  $s^{-1}$ ) which is a function of the within canopy wind speed,  $u_z$  at height above ground,  $z$ . This  
<sub>115</sub> assumes the hydrometeors are following fluid points in the atmosphere.

## <sub>116</sub> 3 Data and methods

### <sub>117</sub> 3.1 Study site

<sub>118</sub> This study was conducted at Fortress Mountain Research Basin (FMRB), Alberta, Canada,  
<sub>119</sub> -115° W, 51° N, a continental headwater basin in the Canadian Rockies (Figure 1). Data from  
<sub>120</sub> this study was collected between October 2021 and July 2023 within and surrounding two  
<sub>121</sub> forest plots adjacent to the FMRB Powerline Station (PWL) and Forest Tower Station (FT)  
<sub>122</sub> at ~2100 m above sea level as shown in Figure 1. The average annual precipitation at PWL  
<sub>123</sub> Station from 2013 to 2023 was 1045 mm, with the peak annual snow water equivalent (SWE)  
<sub>124</sub> reaching 465 kg m<sup>-2</sup>, typically occurring in late April. The PWL and FT forest plots include  
<sub>125</sub> discontinuous stands of 70% subalpine fir (*Abies lasiocarpa*) and 30% Engelmann spruce (*Picea*  
<sub>126</sub> *engelmannii*) (Langs et al., 2020). The PWL plot is located 120 m to the northwest of FT  
<sub>127</sub> station and contains a forest clearing with a diameter of ~12 m, surrounded by a closed canopy.  
<sub>128</sub> The canopy coverages of the two forest plots are 0.51 and 0.29 and the winter leaf area indices  
<sub>129</sub> are 2.07 and 1.66 for PWL and FT respectively. The average height of the canopy surrounding  
<sub>130</sub> the plot to the east of the PWL station is 10.5 m and surrounding the forest plot around the  
<sub>131</sub> FT Station is 7.1 m. The forest of the FT plot has a discontinuous canopy without artificial  
<sub>132</sub> clearings. In August of 1936, the majority of vegetation in FMRB burned during a large forest  
<sub>133</sub> fire that affected most of the Kananaskis Valley (Fryer et al., 1988). Following the fire, the  
<sub>134</sub> forest within the PWL and FT forest plots has naturally regenerated, though some trees have  
<sub>135</sub> been removed for road clearing and creation of a snow study plot.

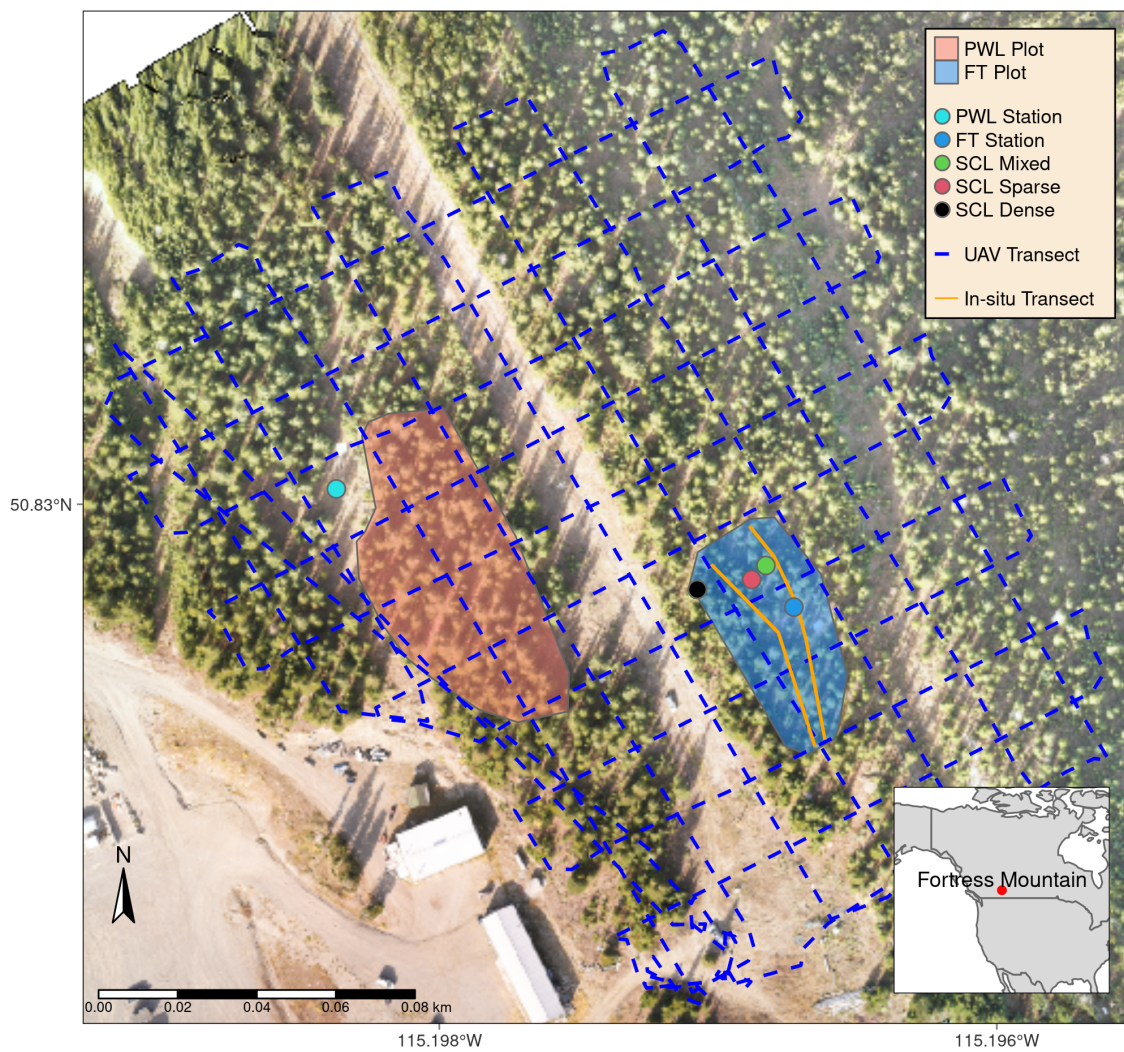


Figure 1: Map showing the location of forest plots, flux towers, subcanopy lysimeter instruments (SCL), and survey transects. The inset map on the lower right shows the regional location of Fortress Mountain Research basin.

<sup>136</sup> **3.2 Meteorological measurements**

<sup>137</sup> Measurements of air temperature and relative humidity (Vaisala model HMP155A), wind speed  
<sup>138</sup> and direction (RM Young model 86000 2-D ultrasonic anemometer) were made 4.3 m above  
<sup>139</sup> the ground at FT station (Figure 1). Wind speed measurements from a 3-cup anemometer  
<sup>140</sup> (Met One model 014A), installed adjacent to the 2-D ultrasonic anemometer at 4.3 m, were  
<sup>141</sup> used for gap filling wind speed. Additional wind speed measurements were collected by two 3D  
<sup>142</sup> sonic anemometers (Campbell Scientific CSAT3) installed at 2 m (raised to 3 m February 2022)  
<sup>143</sup> and 13.5 m above the ground at FT station. Average wind speeds at these four heights were  
<sup>144</sup> found to follow a logarithmic relationship for periods where the instruments were known to be  
<sup>145</sup> clean of snow. Thus, a wind profile was fitted to these measurements using the Prandtl-von  
<sup>146</sup> Kármán log-linear relationship:

$$\bar{u} = \frac{u_*}{k} \ln\left(\frac{z - d_0}{z_0}\right) \quad (5)$$

<sup>147</sup> where  $\bar{u}$  is average wind speed ( $\text{m s}^{-1}$ ) at height,  $z$  (m) above the ground,  $u_*$  is the friction  
<sup>148</sup> velocity ( $\text{m s}^{-1}$ ),  $d_0$  is the displacement height (m),  $z_0$  is the roughness length of momentum  
<sup>149</sup> (m), and  $k$  is the dimensionless von Kármán Constant (0.4).

<sup>150</sup> To determine the displacement height and roughness length parameters the function “optim”  
<sup>151</sup> from the stats R package (R Core Team, 2024) was used. The parameters found for the wind  
<sup>152</sup> speed profile include a roughness length of 0.50 m and displacement height of 0.58 m. See  
<sup>153</sup> the supporting information for more information on the development and testing of the wind  
<sup>154</sup> profile. At PWL station, the snowfall rate was measured by an Alter-shielded OTT Pluvio  
<sup>155</sup> weighing precipitation gauge 2.6 m above ground, corrected for undercatch following phase  
<sup>156</sup> correction by Harder & Pomeroy (2013) and catch efficiency by Smith (2007). Wind speed for  
<sup>157</sup> undercatch correction was measured by a 3-cup anemometer (Met One model 014A) at a height  
<sup>158</sup> of 2.6 m at PWL station. An optical disdrometer (OTT Parsivel2) provided measurements  
<sup>159</sup> of hydrometeor particle size and vertical velocity. All measurements were recorded at 15-min

160 intervals using Campbell Scientific dataloggers, except the Parsivel2 which was recorded at  
161 1-minute intervals by an onsite computer.

162 **3.3 Lysimeter measurements**

163 Three subcanopy lysimeters (SCLs) were installed surrounding the FT Station (Figure 1) to  
164 provide 15-minute interval measurements of throughfall as in MacDonald (2010). Figure 2  
165 shows the three SCLs which consisted of a plastic horse-watering trough with an opening of  
166 0.9 m<sup>2</sup> and depth of 20 cm suspended from a load cell (Intertechnology 9363-D3-75-20T1)  
167 attached to an aluminum pipe connected between two trees. For 26 distinct snowfall events,  
168 where canopy snow ablation rates were deemed negligible, the throughfall rate,  $q_{tf}$ , was calcu-  
169 lated by dividing the weight of snow in the SCL by the cross-sectional area of the SCL opening  
170 and determining the rate of change at 15-minute intervals. Canopy snow load was estimated  
171 at the same 15-minute intervals during these events using Equation 1 and incorporating mea-  
172 surements of  $q_{tf}$  from the SCLs and  $q_{sf}$  from the PWL snowfall gauge. Interception efficiency  
173 was also calculated for these intervals using Equation 2. Timelapse imagery, mass change on  
174 a weighed tree lysimeter “hanging tree” (Pomeroy & Schmidt, 1993) and in-situ observations  
175 were used to ensure the ablation of snow intercepted in the canopy was minimal over each inter-  
176 val. Additionally, the  $q_{tf}$  measurements were filtered to include observations with a snowfall  
177 rate  $> 0 \text{ kg m}^{-2} \text{ hr}^{-1}$ , throughfall rate  $> 0.05 \text{ kg m}^{-2} \text{ hr}^{-1}$  and a snowfall rate greater than the  
178 subcanopy lysimeter throughfall rate to minimize observations with unloading. The weighed  
179 tree lysimeter, a live subalpine fir (*Abies lasiocarpa*) tree suspended from a load cell (Artech  
180 S-Type 20210-100) measured the weight of canopy snow load,  $L_{wt}$  (kg). The weight of snow  
181 intercepted on the weighed tree was scaled to an areal estimate of canopy snow load ( $L$ , kg  
182 m<sup>-2</sup>) using measurements of areal throughfall (kg m<sup>-2</sup>) from manual snow surveys and snow-  
183 fall from the PWL Station snowfall gauge (see description of method in Pomeroy & Schmidt,  
184 1993). The canopy structure surrounding three SCLs is shown in Figure 2 and was measured  
185 using hemispherical photography (Nikon Coolpix 4500 and EC-F8 hemispherical lens) and the  
186 hemispheR R package Chianucci & Macek (2023). The leaf area index and canopy coverage

187 from hemispherical photo analysis is shown in Table 1.

Table 1: Canopy structure of the three subcanopy lysimeters (SCL) located proximal to the FT Station. Leaf area index (LAI) and Canopy Coverage was measured using hemispherical photo analysis with the R package hemispheR.

Name	LAI (-)	Canopy Coverage (-)
Sparse	1.59	0.73
Mixed	1.86	0.78
Closed	2.11	0.82

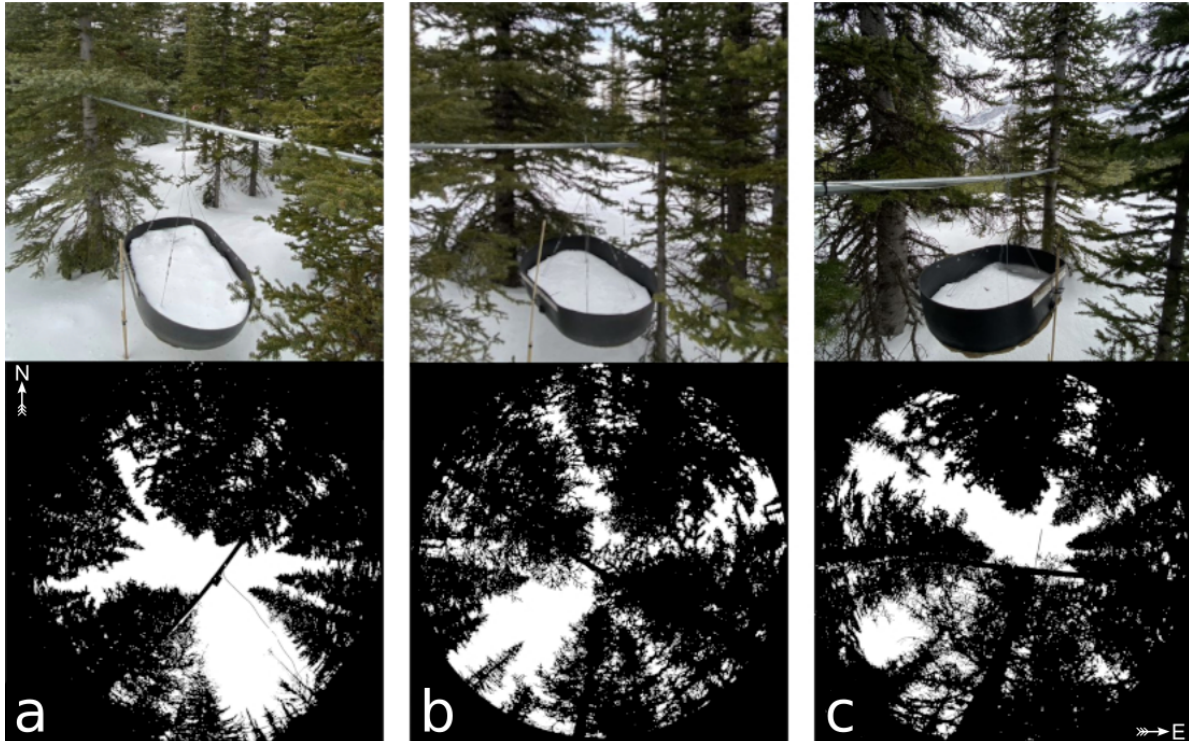


Figure 2: Images of the three subcanopy lysimeters (SCL) and surrounding canopy located in sparse (a), mixed (b), and dense (c) canopy. The top row presents a side view of each SCL and the bottom row shows hemispherical photographs classified using the hemispheR R package. These hemispherical images are oriented with north at the top and have been flipped to provide a view from above (i.e., east is on the right side of each image).

188 **3.4 UAV-Lidar data cCollection and processing**

189 The UAV (FreeFly Alta X) payload included a REIGL miniVUX-2 airborne laser scanner,  
190 an Applanix APX-20 inertial measurement unit (IMU) and global navigation satellite system  
191 (GNSS). The UAV was flown 90 m above the ground at a speed of  $3 \text{ m s}^{-1}$  following the  
192 path shown in Figure 1. A detailed description of the UAV, payload, and flight settings is  
193 provided in the supporting information. The methods outlined by Harder et al. (2020) and  
194 Staines & Pomeroy (2023) were incorporated to reconcile survey lidar, IMU and GNSS data.  
195 A vertical offset of up to 6 cm between UAV-lidar flight lines was observed in the resulting  
196 point clouds on March 13<sup>th</sup> and 14<sup>th</sup>, 2024 and was attributed to IMU position drift. This  
197 offset between flight lines was corrected using the BayesStripAlign software v2.24 (BayesMap  
198 Solutions, 2024). After strip alignment, the mean elevation bias was 0.000 m and the RMS  
199 error declined from 0.055 m to 0.038 m on March 13<sup>th</sup> and changed from 0.033 m to 0.029  
200 m on March 14<sup>th</sup>. The point cloud density ranged from ~1200 returns  $\text{m}^2$  in sparse forest to  
201 ~2200 returns  $\text{m}^2$  in open clearings after flight paths were combined for each survey. Quality  
202 control, ground classification, calculation of the change in between two UAV-lidar point clouds,  
203 and raster generation (0.05 m grid cell resolution) was conducted using the LAStools software  
204 package (LAStools, 2024). Post processing and resampling of raster data to a 0.25 m grid cell  
205 resolution was conducted using the ‘Terra’ R package (Hijmans, 2024). More details on the  
206 UAV-lidar processing workflow are provided in the supporting information.

207 **3.5 Snow surveys**

208 **3.5.1 In-situ snow depth and density**

209 Twelve in-situ fresh snow surveys (six pre- and post-snowfall event pairs) provided measure-  
210 ments of subcanopy throughfall depth and density at 30 locations following the transects shown  
211 in Figure 1 to upscale the weighed tree snow load as in Hedstrom & Pomeroy (1998). Minimal  
212 ablation and redistribution of snow was observed between the pre- and post-snowfall surveys.

When conditions allowed for a UAV-lidar flight, the in-situ snow surveys were conducted following the UAV-lidar flight to assess the accuracy of the throughfall measurements and provide a fresh snow density for the calculation of SWE ( $\text{kg m}^{-2}$ ). A  $1000 \text{ cm}^3$  Perla snow density wedge sampler (RIP Cutter, <https://snowmetrics.com/shop/rip-1-cutter-1000-cc/>) was used to measure the density of the fresh snow layer,  $\overline{\rho_{tf}}$  ( $\text{kg m}^{-3}$ ) from snow pits. Throughfall depth measurements,  $\Delta HS$  were converted to SWE using the following equation:

$$\Delta SWE_{tf} = \Delta HS \cdot \overline{\rho_{tf}} \quad (6)$$

Differential GNSS rover coordinates, with  $\pm 2.5 \text{ cm}$  3D uncertainty, were taken at each snow sampling location so the locations could be queried later from the UAV-lidar rasters to assess measurement error and were also used as input for the UAV-lidar strip alignment. If a pre-event crust layer was present, the depth of post event fresh snow accumulation above the crust layer was interpreted as throughfall over the event. In the absence of a defined crust layer, the difference in pre- and post-event snow depth to ground was interpreted as event throughfall.

### 3.5.2 UAV-Lidar snow depth

Two uncrewed aerial vehicle (UAV) lidar surveys were conducted before and after a 24-hour snowfall event that occurred between March 13<sup>th</sup> and March 14<sup>th</sup>, 2023 to facilitate the measurement of snow accumulation and canopy structure within the FT and PWL forest plots. This period was selected based on two criteria: 1) it provided sufficient cumulative snowfall to result in a low relative error in UAV-LiDAR measured throughfall, and (2) minimal redistribution and ablation was observed, as confirmed by the SCLs, weighed tree, and time-lapse imagery. The change in elevation between the two UAV-lidar surveys was interpreted as the increase in snow accumulation,  $\Delta HS$  over the snowfall event.

<sup>234</sup> **3.6 UAV-Lidar canopy metrics**

<sup>235</sup> To characterize the canopy structure, the voxel ray sampling (VoxRS) methodology for lidar  
<sup>236</sup> data analysis was employed, as developed by Staines & Pomeroy (2023), for the two UAV-  
<sup>237</sup> lidar surveys. This method was chosen for its ability to provide canopy metrics that are less  
<sup>238</sup> sensitive to the inherent non-uniform nature of lidar sampling data, which often results from  
<sup>239</sup> beam occlusion in vegetation and leads to reduced points near the ground. Using this method  
<sup>240</sup> radiation transmittance,  $\tau$  (-), was measured across the hemisphere at a  $1^\circ$  step, i.e., azimuth  
<sup>241</sup> angles ( $0^\circ, 1^\circ, \dots, 359^\circ$ ) and zenith angles ( $0^\circ, 1^\circ, \dots, 90^\circ$ ) for each 0.25 m grid cell within the  
<sup>242</sup> FT and PWL forest plots. The fraction of snow-leaf contact area per unit area of ground  
<sup>243</sup> proposed by Hedstrom & Pomeroy (1998), and hereafter called leaf contact area ( $C_p$ ), was  
<sup>244</sup> then calculated as:

$$C_p(C_c, \theta_h, L) = 1 - \tau \quad (7)$$

$$C_p(C_c, \theta_h, L) = \begin{cases} 1 - \tau, & \text{if } \theta_h > 0^\circ \\ 1 - \tau \approx C_c, & \theta_h = 0^\circ \end{cases} \quad (8)$$

<sup>245</sup> where  $C_p$  is a function of the canopy coverage  $C_c$ ,  $\theta_h$  and  $L$ .  $C_p$  is approximately equal  
<sup>246</sup> to canopy coverage ( $C_c$ ) for vertical snowfall trajectories. However, for non-vertical snowfall  
<sup>247</sup>  $1 > C_p > C_c$ .

<sup>248</sup> **3.7 Statistics and regression models**

<sup>249</sup> To determine how forest structure was associated with interception efficiency at different az-  
<sup>250</sup> imuth and zenith angles over the March 13–14 snowfall event, the entire hemisphere at each  
<sup>251</sup> grid location was considered. The relationship between interception efficiency and canopy  
<sup>252</sup> contact number was found to be linear and thus the Pearson Correlation Coefficient,  $\rho_p$  was

253 calculated using the ‘stats’ package in R (R Core Team, 2024) to quantify the association  
254 between a single raster of interception efficiency and the 32,760 rasters containing the canopy  
255 contact number hemisphere for each portion of the hemisphere (azimuth [0°, 1°, ..., 359°],  
256 zenith angle [0°, 1°, ..., 90°]) for each of the 25 cm grid cells across the FT and PWL forest  
257 plots.

258 Linear and non-linear regression models were developed to assess relationships in the observed  
259 data. Linear models were fitted using ordinary least squares regression via the ‘lm’ function  
260 from the R ‘stats’ package (R Core Team, 2024) to analyze two relationships: (1) between  
261 interception efficiency and meteorological variables and (2) between interception efficiency and  
262 leaf contact area. The latter was forced through the origin based on the theoretical justification  
263 that the dependent variable should be zero when the independent variable is zero. Kozak &  
264 Kozak (1995) noted, the default  $R^2$  value provided for least squares models forced through  
265 the origin by many statistical packages can be misleading. Therefore, these  $R^2$  values were  
266 adjusted using Equation 10 in Kozak & Kozak (1995). Non-linear models were fitted using  
267 non-linear least squares regression via the ‘nls’ function in ‘stats’ package in R.

## 268 4 Results

### 269 4.1 The influence of meteorology on snow interception

270 Canopy snow load was estimated for 26 snowfall events and increased linearly with cumulative  
271 event snowfall without evidence of reaching a maximum (Figure 3). Over these events, air  
272 temperature ranged from -24.5°C to 1°C, wind speeds at 4.3 m height ranged from calm to  
273 4.6 m s<sup>-1</sup> (Table 2), and wind direction was predominately from the southwest during snowfall  
274 (Figure 4). Missing canopy snow load measurements in Figure 3 for certain troughs during  
275 specific events was caused by damage to the subcanopy lysimeter wiring due to animals and  
276 heavy snow loads.

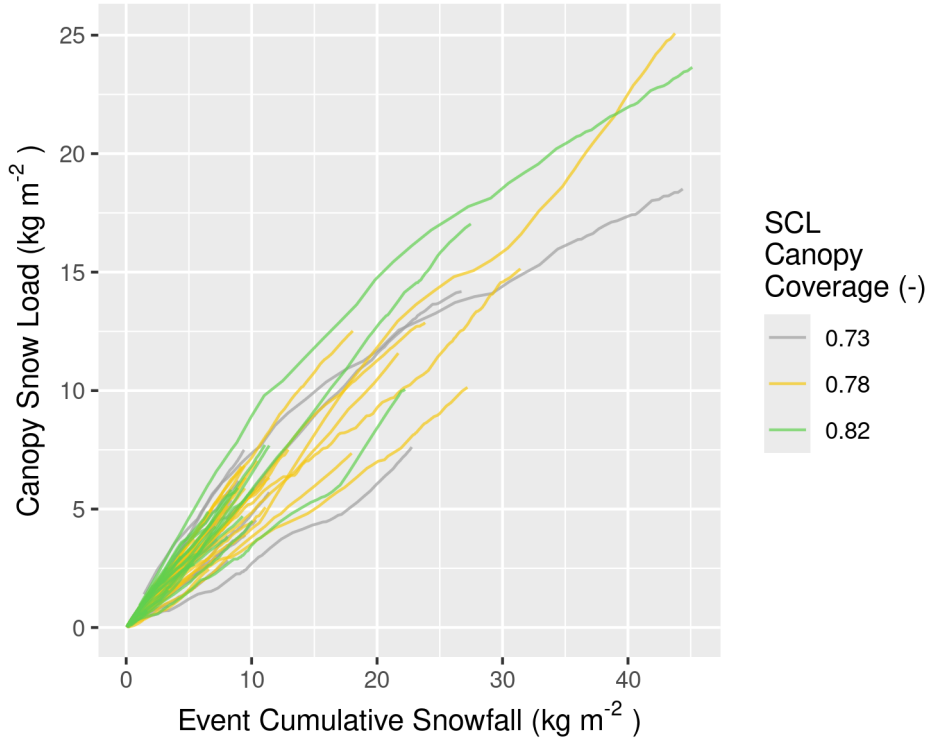


Figure 3: Plot showing the cumulative event snowfall versus the corresponding state of canopy snow load calculated using the SCLs for each of the 26 snowfall events. The SCLs are denoted by a distinct colour (grey, yellow, and green), correspond to varying canopy coverage (0.73, 0.78, and 0.82, respectively).

Table 2: Meteorology of the 26 snowfall events. Air temperature and wind speed were measured at FT station. Snowfall was measured at PWL station. Interception efficiency is estimated from snowfall and the average throughfall of all three SCLs located within the FT forest plot (all from 15-min. measurements).

Start Date	Air Temperature (°C)			Wind Speed (m/s)			Interception Efficiency (-)			Total Snowfall (mm)
	Min	Mean	Max	Min	Mean	Max	Min	Mean	Max	
2021-12-23	-6.2	-5.3	-4.6	0.6	3.1	4.6	0.7	0.8	1.0	21.7
2022-01-02	-15.9	-10.6	-5.8	0.2	1.9	4.2	0.1	0.7	1.0	32.9
2022-01-17	-14.8	-7.8	-0.8	0.2	1.1	1.8	0.0	0.6	1.0	12.9
2022-01-31	-24.5	-12.1	-6.4	0.1	1.0	1.7	0.2	0.7	1.0	9.1
2022-02-14	-9.9	-9.0	-8.5	0.4	0.8	1.2	0.2	0.5	0.8	1.7
2022-02-19	-4.7	-3.2	-2.5	1.3	2.3	3.6	0.3	0.6	0.9	11.1
2022-03-01	-8.3	-5.4	-1.0	0.1	1.0	3.1	0.4	0.8	1.0	9.9
2022-03-07	-12.5	-8.6	-4.4	0.3	0.8	1.7	0.3	0.7	1.0	9.5
2022-03-14	-2.7	-2.1	-0.8	1.0	1.6	2.9	0.2	0.6	0.9	8.4
2022-03-19	-3.1	-2.8	-2.5	0.0	0.7	1.3	0.3	0.5	0.6	6.6
2022-03-23	-7.9	-5.3	-0.9	0.8	1.2	1.8	0.4	0.6	0.9	1.6
2022-04-04	-3.5	-2.9	-2.1	0.6	1.0	1.9	0.0	0.4	0.6	3.4
2022-04-18	-5.2	-4.0	-2.7	0.4	1.1	1.9	0.1	0.5	0.9	7.4
2022-04-22	-2.8	-1.8	-0.5	0.4	0.8	1.2	0.1	0.5	1.0	9.8
2022-05-09	-4.9	-4.3	-3.2	0.1	0.4	0.9	0.2	0.5	0.9	8.1
2022-05-19	-4.9	-2.1	0.3	0.1	0.4	0.9	0.2	0.6	0.9	7.1
2022-06-13	-1.1	-0.3	0.6	0.1	0.1	0.4	0.0	0.5	0.9	45.3
2022-12-27	-3.0	-2.7	-1.9	0.6	1.1	1.8	0.2	0.5	0.9	4.5
2023-01-27	-11.5	-7.3	-4.5	0.6	0.9	1.2	0.1	0.5	0.8	10.4
2023-02-19	-14.3	-9.5	-6.3	0.2	0.8	1.4	0.2	0.7	1.0	18.1
2023-02-26	-9.2	-8.4	-6.6	0.2	1.0	2.1	0.3	0.5	1.0	5.4
2023-03-13	-8.9	-3.6	-0.1	0.3	1.3	2.2	0.0	0.5	1.0	27.4
2023-03-24	-7.9	-5.7	-3.5	0.1	0.5	1.2	0.1	0.4	0.7	23.8
2023-04-01	-8.9	-7.7	-4.7	0.1	0.6	1.4	0.4	0.6	0.8	11.4
2023-04-10	-1.1	-0.5	0.3	0.1	0.3	1.0	0.2	0.4	0.6	18.0
2023-05-08	0.2	0.6	1.0	0.4	0.6	0.8	0.6	0.6	0.7	3.5

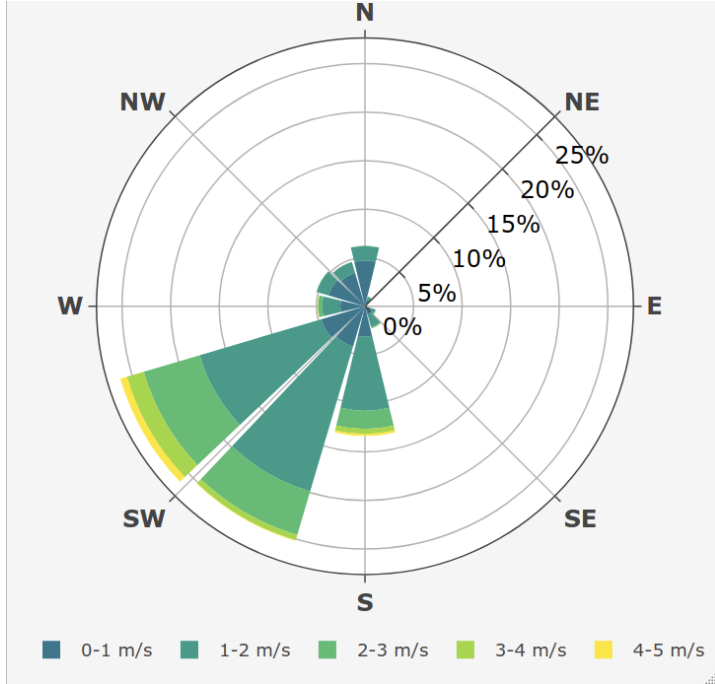


Figure 4: Wind rose showing the frequency of wind speed and direction over the 26 snowfall periods for the ultrasonic anemometer 4.3 m above ground at FT station.

277 Event average air temperature and interception efficiency were negatively associated for the  
 278 mixed canopy ( $R^2 = 0.1$ ,  $p < 0.05$ ), but not associated at the closed and sparse canopies  
 279 (Table 3 & Figure 5). Cumulative event snowfall was not associated with event interception  
 280 efficiency at any site ( $p > 0.05$ ). Event wind speed was positively associated with interception  
 281 efficiency for the sparse ( $R^2 = 0.1$ ,  $p > 0.05$ ) and closed ( $R^2 = 0.2$ ,  $p < 0.05$ ) canopies, both  
 282 with limited canopy openings (Figure 2a,c) towards the prevailing wind direction (Figure 4).  
 283 However, interception efficiency in the mixed canopy, which is open towards the prevailing  
 284 wind direction, was not associated with wind speed ( $p > 0.05$ ).

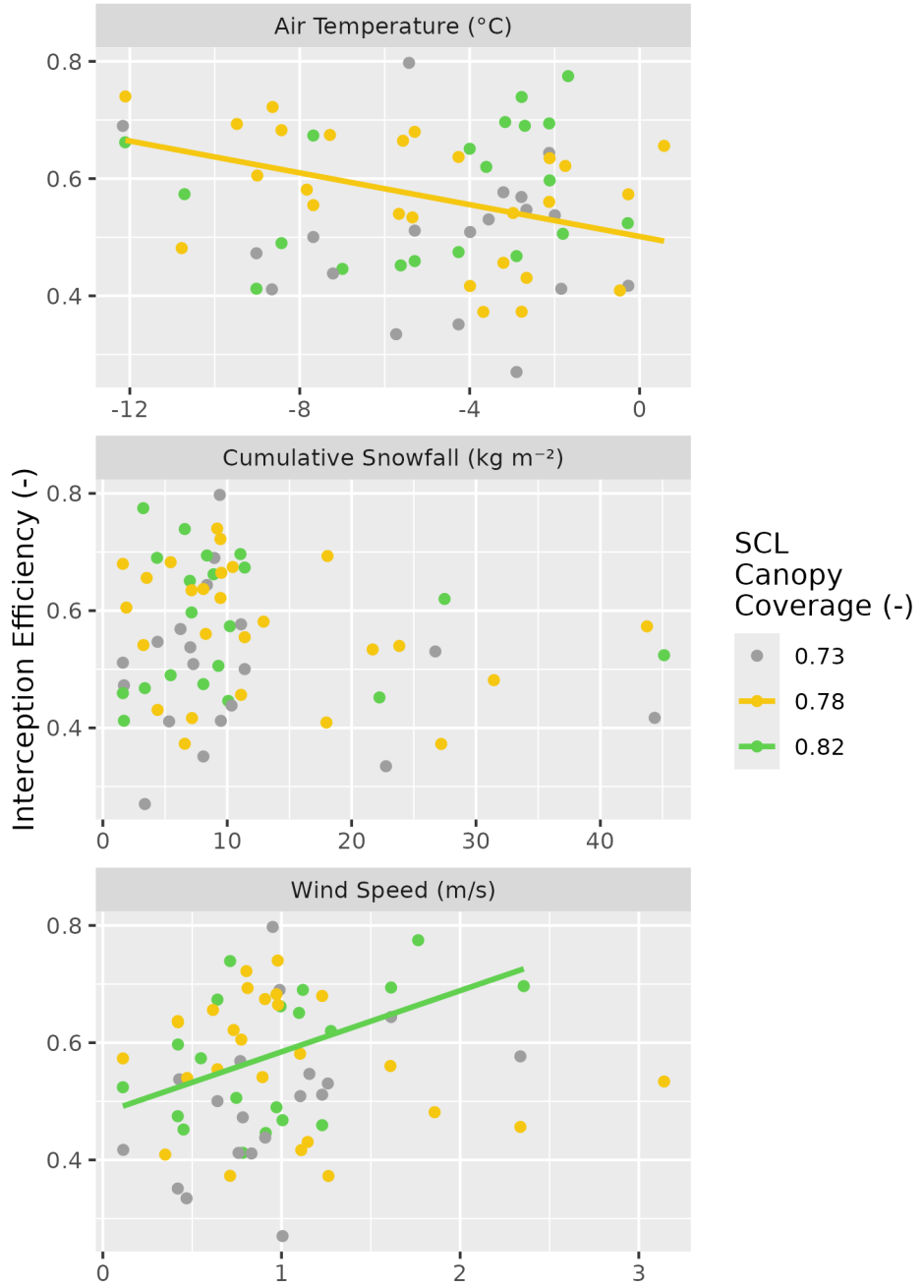


Figure 5: Scatter plots showing the event mean air temperature, mean wind speed, and cumulative snowfall versus the event mean interception efficiency estimated using the SCLs for each of the 26 snowfall events. The colours (grey, yellow, and green), correspond to varying canopy coverage (0.73, 0.78, and 0.82, respectively). A linear regression line fit to the data for significant relationships ( $p < 0.05$ ) is shown by the solid coloured lines. See Table 3 for linear regression statistics.

Table 3: Statistics corresponding to the ordinary least squares linear regression test between independent variables: mean event air temperature, cumulative event snowfall, and mean event wind speed, and the dependent variable mean event interception efficiency. The test was run separately for three levels of canopy coverage ( $C_c$ ).

SCL					
Dependent Variable	Name	$C_c$	Adjusted $R^2$	p-value	n
Air Temperature (°C)	Sparse	0.73	-0.032	0.519	19
Air Temperature (°C)	Mixed	0.78	0.141	0.033	26
Air Temperature (°C)	Closed	0.82	0.008	0.297	20
Cumulative Snowfall (kg m <sup>-2</sup> )	Sparse	0.73	-0.038	0.568	19
Cumulative Snowfall (kg m <sup>-2</sup> )	Mixed	0.78	0.030	0.197	26
Cumulative Snowfall (kg m <sup>-2</sup> )	Closed	0.82	-0.049	0.732	20
Wind Speed (m/s)	Sparse	0.73	0.114	0.087	19
Wind Speed (m/s)	Mixed	0.78	0.010	0.275	26
Wind Speed (m/s)	Closed	0.82	0.192	0.030	20

285 Fifteen-minute interval measurements of interception efficiency and air temperature shown  
 286 in Figure 6a were not associated, despite significant relationships for the sparse and mixed  
 287 canopies ( $R^2 < 0.03$ ,  $p < 0.05$ ), due to low predictive power (Table 4). The average interception  
 288 efficiency across differing bins of air temperature also does not show any systematic trend  
 289 (Figure 6a). However, a significantly greater median interception efficiency ( $p < 0.05$ ) was  
 290 found for binned measurements with air temperatures below -6 °C compared to those with  
 291 warmer air temperatures using non-parametric Wilcoxon signed rank test.

292 Mean wind speed was weakly associated with interception efficiency for the sparse ( $R^2 = 0.1$ ,  $p$   
 293 > 0.05) and closed ( $R^2 = 0.2$ ,  $p < 0.05$ ), but not for the mixed canopy ( $p > 0.05$ ) (Table 4). The  
 294 binned data show an increasing trend in interception efficiency with increasing wind speed for  
 295 the sparse and closed canopies (Figure 6b). A comparison of interception efficiencies binned for  
 296 low (< 1 m s<sup>-1</sup>) and high (> 1 m s<sup>-1</sup>) wind speeds by the Wilcoxon signed rank test, showed that

297 high wind speeds had significantly higher ( $p < 0.05$ ) median interception efficiencies compared  
298 to the low wind speed bins for the closed and sparse canopy. Conversely, the Wilcoxon test  
299 showed the mixed canopy, which had an opening in the canopy towards the prevailing wind  
300 direction (Figure 2b), had significantly higher ( $p < 0.05$ ) median interception efficiencies for  
301 the low wind speed bins.

302 Interception efficiency showed no association ( $R^2 < 0.05$ ,  $p > 0.2$ ) with the canopy load mea-  
303 sured at the beginning of the 15-minute intervals (Table 4). The binned data show a small  
304 increase in interception efficiency for all three canopies when the snow load is less than  $7 \text{ kg m}^{-2}$   
305 (Figure 6c). Interception efficiency later declined for snow loads greater than  $7 \text{ kg m}^{-2}$  for all  
306 canopies, though this was inconsistent for the mixed canopy. A significantly greater ( $p < 0.05$ )  
307 median interception efficiency was found for canopy snow loads less than  $10 \text{ kg m}^{-2}$  than those  
308 with high initial canopy snow loads ( $> 10 \text{ kg m}^{-2}$ ) using the Wilcoxon rank-test. Additional  
309 statistics from ordinary least squares regression test on the 15-minute interval measurements  
310 are provided in Table 4.

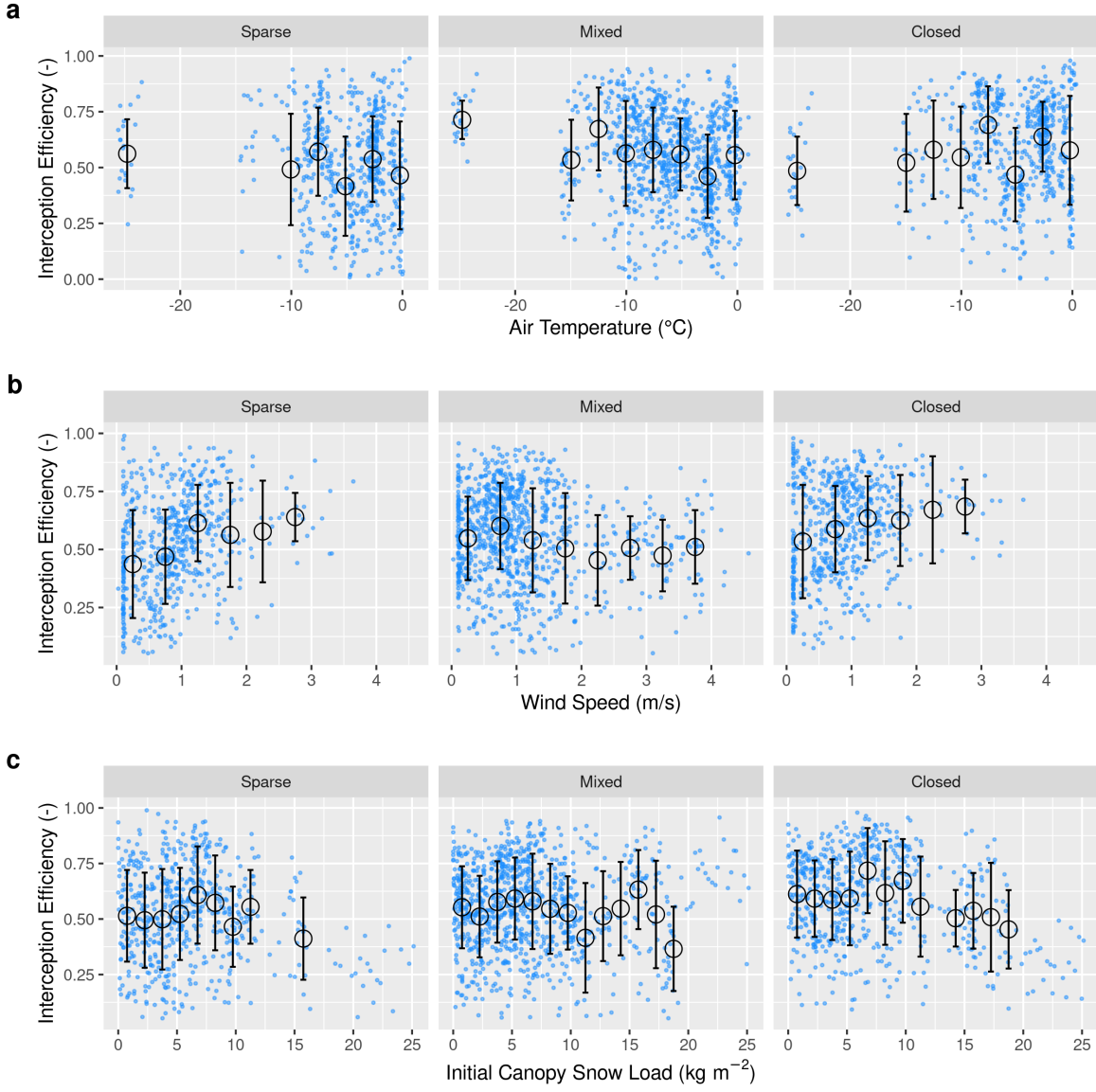


Figure 6: Scatter plots of 15-minute interval measurements (blue dots) and binned data (black open circles with error bars) of mean air temperature, mean wind speed, and initial canopy snow load versus mean snow interception efficiency. Panels show (a) air temperature, (b) wind speed, and (c) initial canopy snow load (the snow load observed at the beginning of the timestep). The black open circles show the mean of each bin and the error bars represent the standard deviations. See Table 4 for linear regression statistics.

Table 4: Statistics corresponding to the ordinary least squares linear regression test between 15-minute interval measurements of independent variables: mean air temperature, mean wind speed, and initial canopy snow load and the dependent variable mean interception efficiency. The test was run separately for three levels of canopy coverage ( $C_c$ ).

Dependent Variable		SCL	$C_c$	Adjusted $R^2$	p-value	n
Air Temperature (°C)	Mixed	0.78	0.032	0.000	985	
Air Temperature (°C)	Closed	0.82	0.004	0.069	618	
Air Temperature (°C)	Sparse	0.73	0.007	0.019	603	
Wind Speed (m/s)	Mixed	0.78	0.017	0.000	985	
Wind Speed (m/s)	Closed	0.82	0.037	0.000	618	
Wind Speed (m/s)	Sparse	0.73	0.089	0.000	603	
Initial Canopy Snow Load (kg m <sup>-2</sup> )	Mixed	0.78	0.000	0.453	972	
Initial Canopy Snow Load (kg m <sup>-2</sup> )	Closed	0.82	0.051	0.000	607	
Initial Canopy Snow Load (kg m <sup>-2</sup> )	Sparse	0.73	0.025	0.000	592	

## 4.2 The influence of forest structure on snow interception

UAV-lidar measurements of throughfall and canopy structure provide insights on how the forest canopy influenced subcanopy snow accumulation during a wind-driven snowfall event between March 13<sup>th</sup> and 14<sup>th</sup> 2023. This event totaled 28.7 kg m<sup>-2</sup> of snowfall at PWL station and was characterized by a transition from low rates of snowfall and air temperatures near 0°C to higher rates of snowfall by late afternoon on March 13<sup>th</sup> coinciding with air temperatures around -2.5 °C. An average wind speed of 1.3 m s<sup>-1</sup> and direction of 188° was observed 4.3 m above the ground at FT Station. Figure 7 shows Cionco's (1965) exponential function was not appropriate for this sparse canopy. The predicted hydrometeor trajectory angles at varying heights, calculated using Equation 4 and the mean observed hydrometeor terminal velocity observed over the event of 0.9 m s<sup>-1</sup> are also shown in Figure 7. An average wind speed of

322 1.6 m s<sup>-1</sup> and direction of 188° was calculated by integrating the wind speed from the surface  
 323 to the mean canopy height of FT plot. The corresponding trajectory angle calculated using  
 324 Equation 4 from this integrated wind speed was 61.5°.

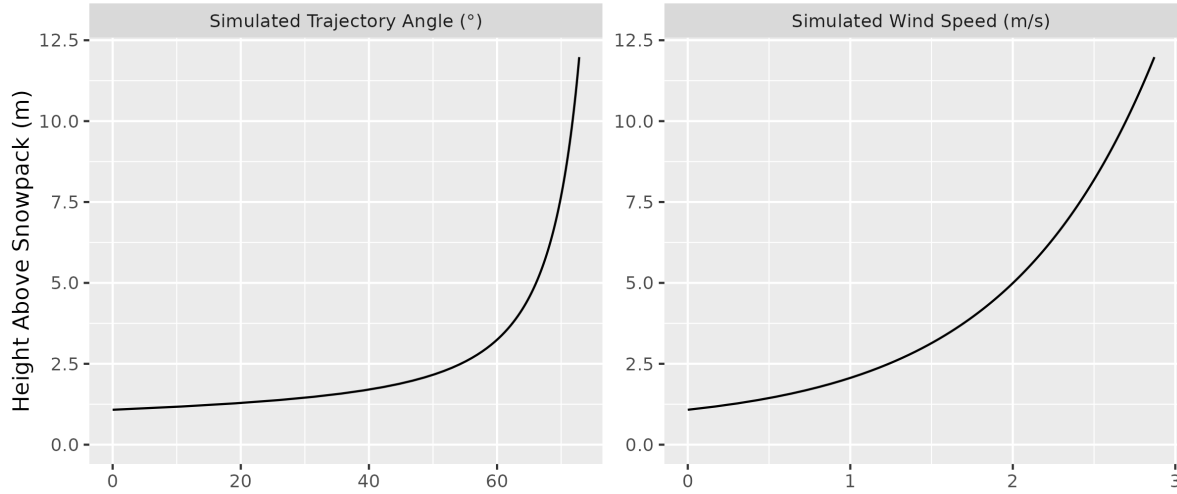


Figure 7: Wind speed profile using roughness length and displacement height parameters derived from anemometers at 2, 3, 4.3, and 13.5 m above ground at FT station over snow free periods and friction velocity estimated over the March 13–14<sup>th</sup> snowfall event.

325 Throughfall depth measured by UAV-lidar was close to the 28 in-situ manual measurements  
 326 with a mean bias of -0.001 m and RMSE of 0.024 m. More details on the accuracy of UAV-lidar  
 327 snowdepth measurements are provided in the supporting information section. Figure 8 shows  
 328 the spatial distribution of throughfall and interception efficiency at the PWL and FT forest  
 329 plots. Reduced throughfall and greater interception efficiency was observed on the north (lee)  
 330 side of individual trees, which may be due to non-vertical hydrometeor trajectories caused by  
 331 the steady southerly winds observed over this event. Transparent areas within the forest plots  
 332 in Figure 8 represent grid cells that did not have any lidar ground returns (i.e., under dense  
 333 canopy proximal to tree trunks) or were masked due to disturbance (i.e., walking paths in  
 334 clearings). Visual observations on March 13<sup>th</sup> and 14<sup>th</sup> confirmed non-vertical hydrometeor  
 335 trajectories and increased canopy snow loads were observed on the windward side of individual

<sup>336</sup> trees. This effect is shown in Figure 8 to be more apparent in the PWL forest plot than the  
<sup>337</sup> FT forest plot. This may be attributed to the taller trees and higher canopy coverage of the  
<sup>338</sup> PWL forest plot compared to the FT forest plot, as for the same trajectory angle a taller tree  
<sup>339</sup> will produce a larger downwind footprint.

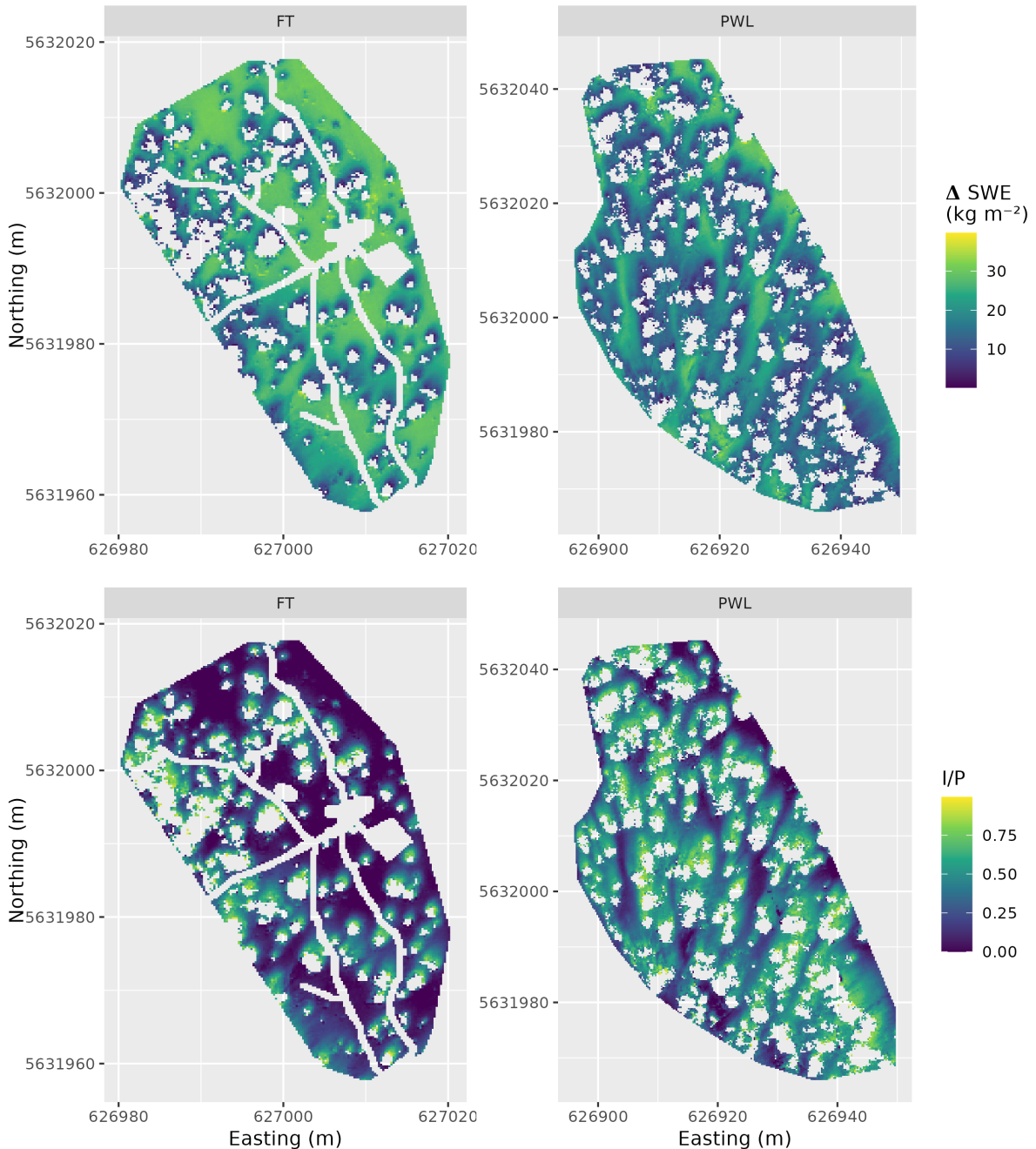


Figure 8: UAV-lidar measurements of the change in snow water equivalent, SWE ( $\text{kg m}^{-2}$ ) and interception efficiency, I/P (-), over the March 13, 2023 24-hour snowfall event for the FT and PWL forest plots at a 0.25 m resolution. See the location of the two forest plots in Figure 1.

340 Figure 9 shows a strong linear correlation between  $C_p$  and interception efficiency towards the  
 341 southern portion of the hemisphere, aligning with the average event wind direction. For the  
 342 PWL forest plot, the upper 97.5<sup>th</sup> percentile of the  $\rho_p$  values shown in Figure 9, were found  
 343 between azimuth angles of 167° – 217°. Similarly, for the FT forest plot, the upper 97.5<sup>th</sup>  
 344 percentile of  $\rho_p$  was found between azimuth angles of 171°–223°. The zenith angle found  
 345 to have the highest correlation over this azimuth range was 22° ( $\rho_p = 0.7$ ) and 21° ( $\rho_p =$   
 346 0.83) for PWL and FT respectively. The high correlation coefficients found for non-vertical  
 347 zenith angles for both PWL and FT are hypothesized to result from non-vertical hydrometeor  
 348 trajectories.

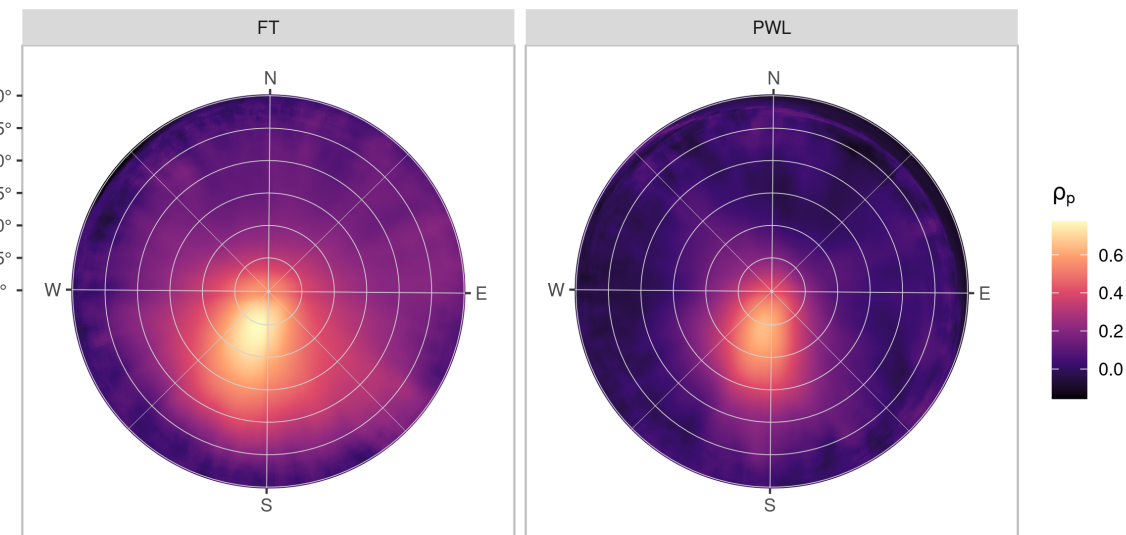


Figure 9: The Pearson Correlation Coefficient between rasters (25 cm resolution) of interception efficiency and leaf contact area for each grid cell across the study site for each azimuth angles (0°, 1°, ..., 359°) and zenith angles (0°, 1°, ..., 90°) for the FT (left) and PWL (right) forest plots.

349 The correlation between  $C_p$  and interception efficiency, resampled to a 5 m grid resolution, was  
 350 higher when  $C_p$  was adjusted for the observed shift in hydrometeor trajectory (Vector Based),  
 351 compared to the leaf contact angle measured at a zenith angle of 0° (nadir) (Figure 10). The  
 352 the zenith angle observed to have the highest  $\rho_p$  in Figure 9 were used to adjust the vector

based,  $C_p$  in Figure 10. The stronger association for the vector-based calculation suggests that adjusted  $C_p$  is a useful predictor of interception efficiency before ablation. An ordinary least squares linear regression forced through the origin was fit to the observed data points using the following equation:

$$\frac{I}{P} = C_p(C_c, \theta_h) \cdot \alpha \quad (9)$$

where  $\alpha$  is an efficiency constant which determines the fraction of snowflakes that contact the  $C_p$  elements and are stored in the canopy (i.e., intercepted) before canopy snow unloading or ablation processes begin.

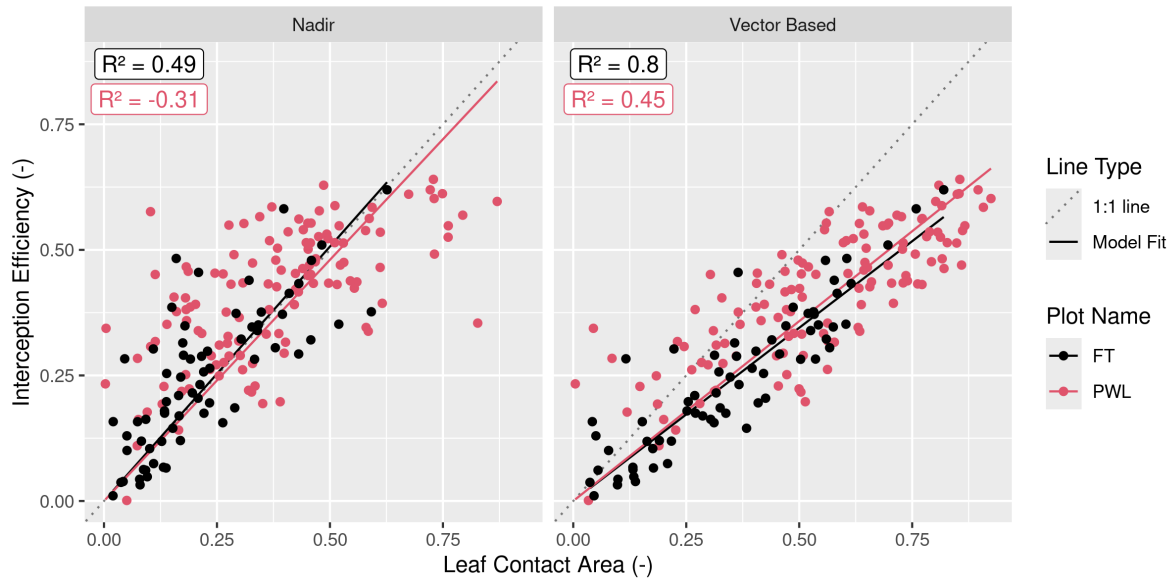


Figure 10: Scatter plots showing the relationship between leaf contact area and interception efficiency rasters resampled to a 5 m grid cell resolution. The left plot (nadir) shows leaf contact area measured from a zenith angle of 0°. The right plot (Vector Based) shows the leaf contact area averaged over rasters with zenith angles (PWL = 22°, FT = 21°) and azimuth angles (PWL = 167°, 178°, ... 217°; FT = 171°, 172°, ... 223°). The solid lines (Model fit) show an ordinary least squares linear regression forced through the origin and fitted to the PWL (red) and FT (black) data and the light grey dotted line shows a 1:1 line. The  $R^2$  values for the four different models are shown in the upper right of each panel calculated following the methods outlined in Kozak & Kozak (1995).

360 For the vector-based model, the relationship between interception efficiency and  $C_p$  results in  
361  $R^2$  values of 0.47 and 0.8 for PWL and FT respectively. The increase in interception efficiency  
362 with  $C_p$  follows a reduced slope compared to the nadir models with  $\alpha$  values of 0.71 and 0.68  
363 for the PWL and FT plots respectively. The reduced slope for the vector-based models may  
364 be due to snowflakes that weaved through and/or bounced off branch elements in addition to  
365 UAV-lidar measurement uncertainty which may have been slightly affected by unloading and  
366 redistribution. These processes would have reduced the fraction of snowfall that was stored  
367 in the canopy. Model error statistics are presented in Table 5 for the nadir and vector-based  
368 models and show the vector-based model provided a better prediction of interception efficiency.  
369 Some of the scatter observed in the nadir model shown in Figure 10 may be explained by grid  
370 cells which observed a greater interception efficiency compared to the corresponding  $C_c$  value  
371 and can be attributed to the inability of  $C_c$  to represent the increase in interception observed  
372 within canopy gaps in Figure 8. Conversely, grid cells where interception efficiency is less than  
373  $C_c$ , may be affected by non-vertical trajectory hydrometeors making their way underneath the  
374 canopy as observed by the reduced interception efficiency on the windward edges of individual  
375 trees in Figure 8. The latter explanation suggests the non-linear relationship observed for the  
376 PWL nadir calculation in Figure 8. The detailed point clouds required to derive the  $C_p$  values  
377 used in this analysis are rarely available and thus more accessible methods to estimate  $C_p$   
378 must be obtained to use Equation 9 which are described in the following section.

Table 5: Model error statistics provided for predictions of interception efficiency using Equation 9 and for different  $a$  values, as shown in the Model Slope column. Statistics are provided for the PWL and FT forest plots, using leaf contact area canopy metrics adjusted to zenith angles of ( $0^\circ, 1^\circ, \dots 30^\circ$ ) and azimuth angles ( $170^\circ, 171^\circ, \dots 220^\circ$ ) and nadir zenith angle of  $0^\circ$ . The Mean bias is the difference in the model and observed values, MAE is the mean of the absolute error, RMS Error is the root mean squared error,  $R^2$  is the coefficient of determination adjusted using Equation 10 in Kozak & Kozak (1995).

Plot	Canopy	Model Slope	Mean Bias	MAE	RMS Error	
Name	Calculation	(-)	(-)	(-)	(-)	$R^2$
FT	Nadir	0.99	0.022	0.071	0.099	0.51
FT	Vector Based	0.68	0.001	0.047	0.062	0.80
PWL	Nadir	0.95	0.048	0.113	0.146	NA
PWL	Vector Based	0.71	0.019	0.078	0.095	0.47

379 **4.3 The combined influence of trajectory angle and forest structure on  
380 interception**

381 Figure 11 shows that  $C_p$ , measured from VoxRS prior to snowfall on March 13<sup>th</sup>, increases  
382 substantially with simulated hydrometeor trajectory angle and corresponding simulated wind  
383 speed. The standard deviation in VoxRS measured  $C_p$ , illustrated by the shaded area in  
384 Figure 11, exhibits the broad range in values for individual grid cells across each forest plot.  
385 Despite this large scatter, a systematic increase in the mean  $C_p$  across both forest plots results  
386 from a rise in the number of canopy elements for more horizontal angles, when averaged across  
387 each forest plot, over all azimuth angles (see top left panel Figure 11). This results in a large  
388 rise in  $C_p$  over relatively common estimated wind speeds. For example, with a wind speed  
389 of  $1 \text{ m s}^{-1}$  and estimated trajectory angle of  $48^\circ$ ,  $C_p$  would increase by 0.31 and 0.28 for the  
390 PWL and FT forest plots respectively (Figure 11). This is a fractional increase in the plot  $C_p$   
391 from nadir of 0.61 and 0.95 for PWL and FT respectively. The increase in  $C_p$  from  $C_c$ , with  
392 increasing trajectory angle is shown on the bottom row of Figure 11 and exhibits a similar

393 relationship for both forest plots FT and PWL until trajectory angles reach approximately  
394  $60^\circ$ . Beyond  $60^\circ$ , the PWL rate of increase slows as the  $C_p$  approaches 1.0, while the FT plot,  
395 which has lower  $C_c$ , continues to rise until around  $75^\circ$  as a  $C_p$  of 1.0 is approached.  $C_p$  was  
396 also quantified across trajectory angles for both PWL and FT on March 14<sup>th</sup>, post snowfall,  
397 and showed a negligible increase in  $C_p$  compared to  $C_p$  measured on March 13<sup>th</sup> without snow  
398 in the canopy.

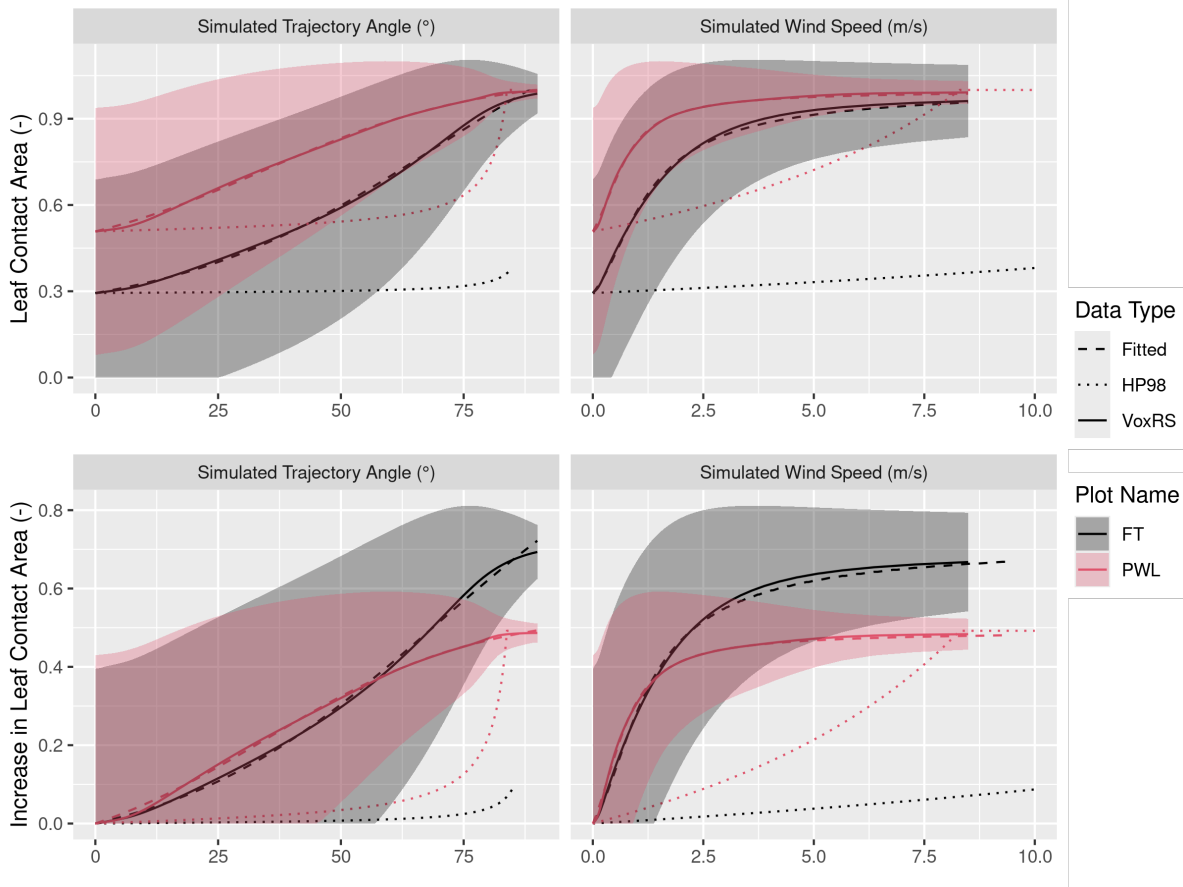


Figure 11: Plots showing the relationship between hydrometeor trajectory angle (left) and wind speed (right) with mean plot-wide snow-leaf contact area,  $C_p$  (top row) and the increase in mean plot-wide  $C_p$ , i.e.,  $C_p - C_c$  (bottom row). The hydrometeor trajectory angle is simulated through VoxRS and is measured as degrees from zenith. Simulated wind speed was calculated as a function of hydrometeor trajectory angle by rearranging Equation 4 and an observed event hydrometeor velocity of  $0.9 \text{ m s}^{-1}$ . The solid lines (VoxRS) represent the mean  $C_p$  (top row) or increase in mean  $C_p$  (bottom row) for a single zenith angle observed from VoxRS across all grid cells for each forest plot and across all azimuth angles. The shaded area represents 1 standard deviation above and below the observed VoxRS mean. The dashed lines (Fitted) represent predictions from Equation 10 (top) and Equation 11 (bottom). The dotted lines (HP98) represent the predictions from Equation 10 in Hedstrom & Pomeroy (1998). A forested downwind distance of 100 m was assumed for the HP98 calculation.

<sup>399</sup> A function is proposed here to calculate plot scale leaf contact area,  $C_p$  (-):

$$C_p = C_c + C_{inc}(\theta_h) \quad (10)$$

400 where,  $C_{inc}$  is the increase in leaf contact area from  $C_c$  which is a function of  $\theta_h$ . To estimate  
 401  $C_{inc}$  a non-linear least squares regression using a logistic function forced through the origin was  
 402 fit to the VoxRS measurements at FT and PWL for simulated hydrometeor trajectory angles  
 403 (see dashed lines in bottom row of Figure 11). A logistic function was selected to model this  
 404 relationship, as its shape reflects the slow increase in observed  $C_p$  at near vertical trajectory  
 405 angles, followed by a rapid increase to represent increase canopy area in the middle and lower  
 406 section of individual trees, and the gradual leveling off as  $C_p$  approaches a value of 1.0. The  
 407 logistic function used to predict  $C_{inc}$  as a function of  $\theta_h$  is:

$$C_{inc} = \left( \frac{C_{inc}^{max}}{1 + e^{\left( \frac{\theta_0 - \theta_h}{k} \right)}} - \frac{C_{inc}^{max}}{1 + e^{\left( \frac{\theta_0}{k} \right)}} \right) \quad (11)$$

408 where  $C_{inc}^{max}$  is the maximum value of  $C_{inc}$ ,  $\theta_0$  is the x-value of the sigmoid midpoint and  $k$  is  
 409 the logistic growth rate or steepness of the curve. The coefficients resulting from the non-linear  
 410 least squares regression fit of Equation 11 to the VoxRS dataset are presented in Table Table 6.  
 411 Simulated  $C_p$  using Equation 10 is shown in the dashed lines in the top row of Figure 11 and  
 412 follows closely to the VoxRS-measured mean  $C_p$ . Model error statistics shown in Table 7  
 413 demonstrate that Equation 11 performed well, with a mean bias and RMSE of 0.001 (-) and  
 414 0.0054 (-) respectively for PWL, and -0.0004 (-) and 0.0079 (-) for FT. In contrast, Table 7  
 415 reveals that the Hedstrom & Pomeroy (1998) method produced significantly less accurate  
 416 estimates of  $C_p$ , with a mean bias and RMSE of -0.201 (-) and 0.233 (-) respectively for PWL,  
 417 and -0.260 (-) and 0.324 (-) for FT.

Table 6: Coefficients derived from the non-linear least squares regression fit of Equation 11 to the VoxRS dataset.

Plot Names	$LCA_{max}$	$\theta_0$	$k$
PWL	0.66	34.58	22.14
FT	1.18	69.13	26.98

Table 7: Model error statistics calculated for the prediction of leaf contact area from trajectory angle using Equation 11 (nls) and Equation 10 from Hedstrom & Pomeroy (1998) for the PWL and FT forest plots. Mean bias is the difference in the model and observed values, MAE is the mean of the absolute error, RMS Error is the root mean squared error and  $R^2$  is the coefficient of determination. The units for all metrics are dimensionless. A forested downwind distance of 100 m was used for the HP98 calculation.

Model	Plot	Mean Bias (-)	MAE (-)	RMS Error (-)	$R^2$
HP98	FT	-0.2598	0.2598	0.3240	0.7196
HP98	PWL	-0.2008	0.2010	0.2326	0.4446
nls	FT	-0.0004	0.0067	0.0079	0.9987
nls	PWL	0.0010	0.0040	0.0054	0.9990

#### 418 4.4 Throughfall model performance

419 The performance of Equations 9, 10, and 11 in estimating event throughfall was assessed  
 420 against UAV-lidar measurements of throughfall for the March 13–14<sup>th</sup> snowfall event at the  
 421 plot scale for both FT and PWL. Required values for the model included the event mean  
 422 hydrometeor terminal velocity and total event snowfall which were measured at PWL station,  
 423 and wind speed was taken as one-third the mean canopy height using the wind speed profile in  
 424 Figure 7. Additional model inputs include the mean  $C_c$  for each plot which was measured from  
 425 the VoxRS dataset. An  $\alpha$  value of 0.836 (-) was found through calibration which provided the

<sup>426</sup> best fit between observed and simulated interception efficiency at the plot scale for both FT  
<sup>427</sup> and PWL.

<sup>428</sup> Figure 12 shows the vector-based model, computed using Equation 9 with  $C_p$  adjusted for  
<sup>429</sup> estimated hydrometeor trajectory angle, closely matches UAV-lidar measurements of through-  
<sup>430</sup> fall. Observed and modelled values of interception efficiency and  $\Delta SWE_{tf}$  are presented in  
<sup>431</sup> Table 8 along with corresponding error statistics. Modelled throughfall from the vector-based  
<sup>432</sup> model was  $17 \text{ kg m}^{-2}$  compared to the measured throughfall of  $16.6 \text{ kg m}^{-2}$  for PWL. For FT,  
<sup>433</sup> the modelled throughfall was  $21.8 \text{ kg m}^{-2}$ , while the measured values were  $22.1 \text{ kg m}^{-2}$ . The  
<sup>434</sup> vector-based model shows a lower mean bias of  $-0.3 \text{ kg m}^{-2}$  for PWL and a negative bias of  
<sup>435</sup>  $0.3 \text{ kg m}^{-2}$  for FT, compared to the larger mean bias of  $-1.6 \text{ kg m}^{-2}$  for PWL and  $-0.8 \text{ kg m}^{-2}$   
<sup>436</sup> for FT with the nadir-model (calculated using  $C_c$  in place of  $C_p$ ). This resulted in a large  
<sup>437</sup> reduction in the percent error in predicted throughfall, from  $-9.4\%$  with the nadir-model to  
<sup>438</sup>  $-1.8\%$  with the vector-based model for PWL. A smaller improvement was observed for FT,  
<sup>439</sup> with the percent error in predicted throughfall declining from  $-3.6\%$  with the nadir-model to  
<sup>440</sup>  $-1.4\%$  with the vector-based model.

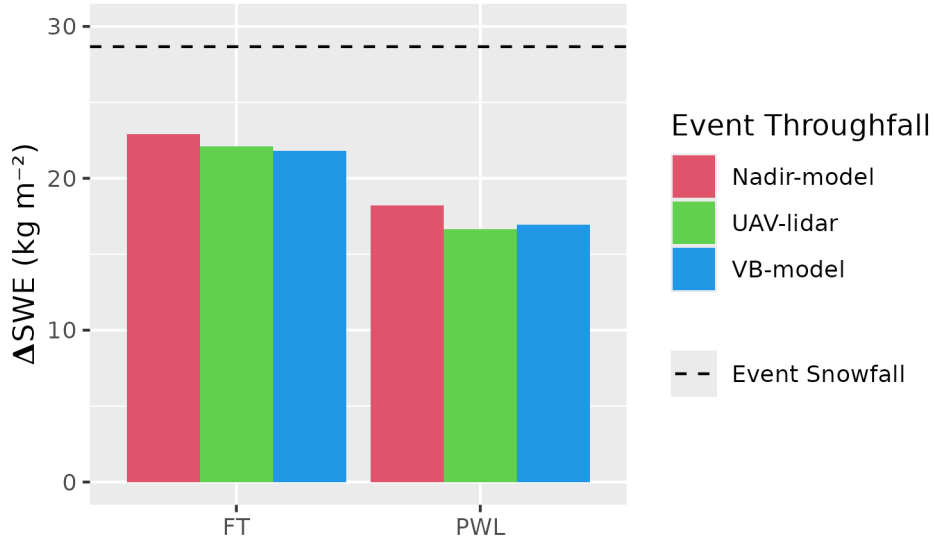


Figure 12: Bar chart comparing the observed and modelled mean change in throughfall (SWE,  $\text{kg m}^{-2}$ ) over the March 13-14 snowfall event averaged over forest plots FT and PWL. The ‘Nadir-model’ used Equation 9 not adjusted for trajectory angle (i.e.,  $C_c$ ) and the Vector-based ‘VB-model’ which uses Equation 9 with  $C_p$  adjusted for trajectory angle. ‘UAV-lidar’ corresponds to throughfall calculated using Equation 6 incorporating UAV-lidar snow depth and snow density from in-situ snow pits. The black horizontal dashed line shows the accumulated SWE ( $\text{kg m}^{-2}$ ) over the snowfall event to the PWL station open clearing.

Table 8: Model error statistics for model estimates of snow interception efficiency (I/P) and throughfall (TF) compared to measurements of I/P and TF using UAV-lidar averaged over the FT and PWL forest plots. Units for I/P are (-) and TF are ( $\text{kg m}^{-2}$ ). The vector-based model utilized Equation 9 with  $C_p$  adjusted for trajectory angle. The nadir model also utilized Equation 9 but was not adjusted for trajectory angle and thus  $C_c$  was used instead of  $C_p$ . The ‘Obs. Value’ column contains measurements from UAV-lidar while the ‘Mod. Value’ column contains the modelled values. The mean bias was calculated as observed minus modelled and percent error is the percent error between predicted and observed values.

Plot	Type	Model	Value	Units	Obs.	Mod.	Mean	
		Name			Value	Value	Bias	Perc. Error
FT	VB-model	I/P	-		0.23	0.24	-0.01	-4.67
FT	Nadir-model	I/P	-		0.23	0.20	0.03	12.10
FT	VB-model	TF	$\text{kg m}^{-2}$		22.12	21.82	0.31	1.38
FT	Nadir-model	TF	$\text{kg m}^{-2}$		22.12	22.91	-0.79	-3.58
PWL	VB-model	I/P	-		0.42	0.41	0.01	2.54
PWL	Nadir-model	I/P	-		0.42	0.37	0.05	12.95
PWL	VB-model	TF	$\text{kg m}^{-2}$		16.64	16.95	-0.31	-1.84
PWL	Nadir-model	TF	$\text{kg m}^{-2}$		16.64	18.20	-1.56	-9.35

## 441 5 Discussion

442 The point scale observations presented in Figure 6 show air temperature had little influence  
 443 on interception efficiency. This differs from existing studies which suggested either a positive  
 444 (Storck et al., 2002) or negative (Hedstrom & Pomeroy, 1998) relationship. A weak relation-  
 445 ship, that leaves 80–90% of variance unexplained, was observed between initial interception

<sup>446</sup> efficiency (before unloading) with increasing wind speed at two locations which were sheltered  
<sup>447</sup> from the predominant wind direction (Figure 6b). This is attributed to an associated increase  
<sup>448</sup> in  $C_p$  due to non-vertical hydrometeor trajectories. These results are consistent with observa-  
<sup>449</sup> tions by Schmidt & Troendle (1989) who observed a slight increase in snowfall interception  
<sup>450</sup> with increasing wind speeds up to  $6 \text{ m s}^{-1}$  and studies of rainfall interception by Herwitz &  
<sup>451</sup> Slye (1995) and Van Stan et al. (2011).

<sup>452</sup> Compared to the influence of wind speed, interception efficiency showed a smaller sensitivity  
<sup>453</sup> to canopy snow load at the point scale (Figure 5). The slight increase in interception efficiency  
<sup>454</sup> for smaller canopy snow loads and decline for larger canopy snow loads is attributed to the  
<sup>455</sup> influence of canopy snow load on  $C_p$  (Figure 6c). While small, this effect is consistent with  
<sup>456</sup> the theory proposed by Satterlund & Haupt (1967) that interception efficiency increases as  
<sup>457</sup> the canopy fills with snow bridging gaps in the canopy increasing, while later declining due to  
<sup>458</sup> branch bending and decreased canopy coverage. However, the observations shown in Figure 6  
<sup>459</sup> and Figure 3, which minimized ablation processes, differ from those reported by Satterlund  
<sup>460</sup> & Haupt (1967), Schmidt & Pomeroy (1990), and Moeser et al. (2015), as canopy snow load  
<sup>461</sup> increased linearly with snowfalls up to  $45 \text{ kg m}^{-2}$  without approaching a maximum canopy snow  
<sup>462</sup> load. The strong exponential decline in interception efficiency with increasing event snowfall  
<sup>463</sup> in these studies Schmidt & Pomeroy (1990) may have resulted from higher unloading rates as  
<sup>464</sup> branches bent under heavy snow loads, hence mixing ablation and interception processes to  
<sup>465</sup> varying degrees. In contrast, other studies (Calder, 1990; Watanabe & Ozeki, 1964) align with  
<sup>466</sup> the observations in Figure 6 and Figure 3, showing little evidence of a reduced interception  
<sup>467</sup> efficiency with increasing snowfall. The low sensitivity of interception efficiency with canopy  
<sup>468</sup> snow load found in this study and others may be attributed to several factors: a reduced  
<sup>469</sup> inclusion of ablation processes in the interception efficiency measurements, limited influence  
<sup>470</sup> of canopy snow load on  $C_p$  at this study site, and/or the compensatory effects outlined by  
<sup>471</sup> Satterlund & Haupt (1967).

<sup>472</sup> Staines & Pomeroy (2023) showed a slight increase in VoxRS  $C_p$  between snow-off and snow-on  
<sup>473</sup> conditions. However, the increase in  $C_p$  resulting from snow load in Staines & Pomeroy (2023)

474 was small compared to the substantial rise in  $C_p$  due to trajectory angle presented in their  
475 study and as shown in Figure 11. Both findings from Staines & Pomeroy (2023) corroborate  
476 the results reported in this study. Further evidence in support of the relatively small influence  
477 of canopy snow load on  $C_p$ , is provided by Lundquist et al. (2021) who reported improved  
478 simulation of subcanopy snow accumulation without the use of a maximum canopy snow load,  
479 when linked with a comprehensive canopy snow ablation routine. Lehtonen et al. (2016)  
480 also note that in northern Finland heavy canopy snow loads have been observed to continue  
481 increasing until stem breakage, under conditions favourable for the formation of significant  
482 rime-ice accretion and limited ablation, thus reducing  $C_p$ . Models are available to predict the  
483 accretion of ice on tree canopies (e.g., Nock et al., 2016) however, further research is required  
484 to understand the canopy snow load required to cause stem breakage across different tree  
485 species and canopy loads.

486 These findings on the limited influence of air temperature and canopy snow load on initial  
487 interception challenge the theoretical basis of many existing snow interception parameteriza-  
488 tions (Hedstrom & Pomeroy, 1998; Moeser et al., 2015; Satterlund & Haupt, 1967; Storck et  
489 al., 2002). To address this a new snow interception parameterization, Equation 9, is presented  
490 which calculates interception efficiency as a function of  $C_p$  and  $\alpha$ . This new parameterization  
491 allows for canopy snow loading processes to be isolated from canopy snow ablation processes  
492 and is consistent with current rainfall interception theory (Valante et al., 1997). Equation 9  
493 differs only slightly from the original Hedstrom & Pomeroy (1998) parameterization (see Equa-  
494 tion 6 in Hedstrom & Pomeroy (1998)), in that it does not calculate interception efficiency  
495 as a function of canopy snow load and from the Storck et al. (2002) parameterization who  
496 proposed interception efficiency to be constant over time and space. The theoretical basis of  
497 the  $\alpha$  parameter in Equation 9 is that the association between  $C_p$  and interception efficiency,  
498 as shown in Figure 10, unlike existing rainfall parameterizations (Valante et al., 1997) does not  
499 follow a 1:1 line, as falling snow hydrometeors may bounce off the canopy elements. Further  
500 research is needed to explore how processes such as the increased cohesion and adhesion of  
501 snowfall to the canopy at warm temperatures, as observed by Kobayashi (1987), Pfister &

502 Schneebeli (1999), Storck et al. (2002), as well as hydrometeor velocity, particle size, and  
503 shape suggested by (Katsushima et al., 2023), may influence the  $\alpha$  parameter, although these  
504 effects were not observed in this study.

505 Measurements of interception efficiency and canopy structure, as shown in Figure 8, align with  
506 the theory proposed by Hedstrom & Pomeroy (1998) which suggests reduced throughfall on  
507 the lee side of individual trees. However, an existing method proposed in Hedstrom & Pomeroy  
508 (1998) to scale canopy coverage with wind speed failed to reproduce the observations presented  
509 in Figure 11. A new method is proposed which uses a logistic function to calculate plot-wide  
510  $C_{inc}$  as a function of  $\theta_h$  and  $C_c$ . Significant scatter in VoxRS measured  $C_p$  across the two  
511 forest plots, illustrated by the high standard deviation in Figure 11, resulted from directional  
512 (azimuth) and spatial differences in canopy structure. This large scatter suggests the observed  
513 relationships in Figure 11 are only applicable at the forest stand scale where the sub-metre  
514 variability in  $C_p$  averages out. At the point scale, the mixed canopy SCL which is open to the  
515 prevailing wind direction (Figure 2), and did not follow this relationship and led to an increase  
516 in throughfall with increasing wind speed (Figure 5 & Figure 6). However, Figure 11 shows  
517 that at the plot scale,  $C_p$  rises with increasing  $\theta_h$ , as there is a greater number of grid cells  
518 which have more closed canopy at more horizontal angles. Thus at the plot scale, Equation 11,  
519 which uses trajectory angle alone, was shown to successfully determine  $C_{inc}$  and thus  $C_p$  for  
520 the discontinuous canopies of both the FT and PWL forest plots. However, Equation 11 would  
521 not be applicable to areas that have large continuous gap fractions (e.g., large forested clear  
522 cuts) that are many times wider than the mean canopy height. Further work is required to  
523 refine the relationship proposed in Equation 11 across a range of tree species and densities.  
524 Backflows and large eddies that occur within the canopy may also contribute to very mixed  
525 responses (Staines & Pomeroy, 2023).

526 It was found that the mean hydrometeor trajectory angle over a snowfall event, required for  
527 Equation 11, could be predicted by using the observed hydrometeor fall velocity and a mean  
528 horizontal wind speed selected at one-third of the canopy height above the ground. A wind  
529 speed at one-third the mean canopy height is hypothesized to be important for canopy snow

530 accumulation as a large fraction of the horizontal cross-sectional area is at this height for most  
531 needleleaf canopies. Katsushima et al. (2023), also proposed the wind speed at one-third the  
532 canopy height for modelling unloading of canopy snow as it corresponds to the centre of gravity  
533 when the horizontal projection of the canopy is assumed to be a triangle. However, there is  
534 uncertainty in the transferability of the canopy height observed here to other environments  
535 due to differing tree structures and tree species. This may include forests with a larger trunk  
536 space or have more of their canopy contact area at higher heights above the ground (i.e., some  
537 deciduous canopies). Moreover, Equation 4 assumes a linear hydrometeor trajectory, and does  
538 not consider non-linear patterns such as wind flow directions around tree elements, turbulent  
539 flow, or differences in wind speed with height.

540 Although the improvement in performance of the vector-based model over the nadir model was  
541 relatively small, the vector-based model is preferred due to its overall lower error compared  
542 to the UAV-lidar measurements and better representation of physical processes. While the  
543 vector-based model acts to increase interception efficiency with wind speed, several studies  
544 have shown that canopy snow ablation increases as a result of wind induced unloading (Bartlett  
545 & Verseghy, 2015; Betts & Ball, 1997; Lumbrazo et al., 2022; Roesch et al., 2001; Wheeler,  
546 1987). Thus, representing both the increase in initial interception due to inclined hydrometeor  
547 trajectory angles and the subsequent increase in canopy snow unloading will be important in  
548 subcanopy snow accumulation models.

## 549 **6 Conclusions**

550 New observations of initial snow interception, collected over a wide range of meteorological  
551 conditions and canopy structures suggest forest structure is the primary factor governing  
552 subcanopy snow accumulation. At the point scale, high-temporal resolution measurements  
553 revealed no evidence of a maximum canopy snow load, even for event snowfalls up to 45 kg  
554 m<sup>-2</sup>, nor was there any indication of air temperature influencing the cohesion and adhesion of  
555 snowfall to the canopy or branch bending reducing canopy coverage. Instead, wind speed was

556 found to influence interception efficiency by changing the hydrometeor trajectory angle, which  
557 can lead to a substantial increase in snow-leaf contact area.

558 At the forest plot scale, UAV-lidar measurements of throughfall collected over a wind-driven  
559 snowfall event confirmed the results observed at the point-scale and showed leaf contact area  
560 was the main factor governing the interception efficiency at a particular site. The leaf contact  
561 area, which accounts for the change in canopy structure with trajectory angle, proved to be  
562 a better predictor of interception efficiency compared to nadir-calculated canopy coverage.  
563 When averaged across each forest plot, leaf contact area was shown to be highly sensitive to  
564 hydrometeor trajectory angle, increasing by 61–95% for trajectory angles associated with a  
565 1 m s<sup>-1</sup> wind speed. An existing theoretical relationship failed to adequately represent the  
566 VoxRS-measured increase in leaf contact area with simulated trajectory angles. As a result, a  
567 new relationship is proposed, which demonstrated good performance at this study site.

568 The weak association between air temperature and canopy snow load with interception effi-  
569 ciency, as presented here and in other recent studies, coupled with the considerable influence  
570 of wind speed on leaf contact area, highlights the need for a new snow interception parameter-  
571 ization. A new parameterization is proposed that calculates initial interception as a function  
572 of snowfall and leaf contact area. This parameterization is consistent with many rainfall in-  
573 terception studies, which also separate canopy loading and ablation processes, and calculate  
574 interception as a function of canopy coverage. Additionally, a second equation is proposed  
575 to estimate leaf contact area as a function of hydrometeor trajectory angle and nadir canopy  
576 coverage. This updated snow interception parameterization showed good performance in the  
577 subalpine forest in this study, but further validation should be conducted in a range of climates,  
578 forest species, and canopy structures.

## 579 **7 Acknowledgments**

580 We wish to acknowledge financial support from the University of Saskatchewan Dean's Schol-  
581 arship, Natural Sciences and Engineering Research Council of Canada, Global Water Futures

582 Programme, Environment and Climate Change Canada, Alberta Innovates, Canada Founda-  
583 tion for Innovation, and the Canada Research Chairs Programme. We thank Madison Harasyn,  
584 Hannah Koslowsky, Kieran Lehan, Lindsey Langs and Fortress Mountain Resort for their help  
585 in the field. Jacob Staines, Madison Harasyn, Alistair Wallace, and Rob White contributed  
586 to developing the UAV-lidar processing workflow.

## 587 **8 Data Availability**

588 The data that support the findings in this study are available at <https://doi.org/10.5281/zenodo.14018893>.

589 **9 References**

- 590 Axelsson, P. (2000). Peter Axelsson 110. *International Archives of Photogrammetry and*  
591 *Remote Sensing*, 33(4), 110–117. [https://www.isprs.org/proceedings/XXXIII/congress/part4/111\\_XXXIII-part4.pdf](https://www.isprs.org/proceedings/XXXIII/congress/part4/111_XXXIII-part4.pdf)
- 592 Bartlett, P. A., & Verseghy, D. L. (2015). Modified treatment of intercepted snow improves  
593 the simulated forest albedo in the Canadian Land Surface Scheme. *Hydrological Processes*,  
594 29(14), 3208–3226. <https://doi.org/10.1002/HYP.10431>
- 595 BayesMap Solutions. (2024). *BayesStripAlign*. <https://bayesmap.com/products/bayesstripalign/>
- 596 Betts, A. K., & Ball, J. H. (1997). Albedo over the boreal forest. *Journal of Geophysical*  
597 *Research: Atmospheres*, 102(D24), 28901–28909. <https://doi.org/10.1029/96JD03876>
- 598 Calder, I. R. (1990). *Evaporation in the uplands* (p. 148). Wiley.
- 599 Cebulski, A., & Pomeroy, J. W. (2024). The theoretical underpinnings of snow interception  
600 and ablation parameterizations. *Wiley Interdisciplinary Reviews: Water, In Review*.
- 601 Chianucci, F., & Macek, M. (2023). hemispheR: an R package for fisheye canopy image  
602 analysis. *Agricultural and Forest Meteorology*. <https://doi.org/10.1016/j.agrformet.2023.109470>
- 603 Cionco, R. M. (1965). A Mathematical Model for Air Flow in a Vegetative Canopy. *Journal of*  
604 *Applied Meteorology* (1962), 4(4), 517–522. [https://doi.org/10.1175/1520-0450\(1965\)004%3C0517:AMMFAF%3E2.0.CO;2](https://doi.org/10.1175/1520-0450(1965)004%3C0517:AMMFAF%3E2.0.CO;2)
- 605 Clark, M. P., Nijssen, B., Lundquist, J. D., Kavetski, D., Rupp, D. E., Woods, R. A., Freer,  
606 J. E., Gutmann, E. D., Wood, A. W., Gochis, D. J., Rasmussen, R. M., Tarboton, D. G.,  
607 Mahat, V., Flerchinger, G. N., & Marks, D. G. (2015). A unified approach for process-  
608 based hydrologic modeling: 2. Model implementation and case studies. *Water Resources*  
609 *Research*, 51(4), 2515–2542. <https://doi.org/10.1002/2015WR017200>
- 610 Clark, M. P., Wood, A., Nijssen, B., Bennett, A., Knoben, W., & Lumbrazo, C. (2020).  
611 *SUMMA v3.0.3*. Zenodo. <https://doi.org/10.5281/zenodo.4558054>

- 617 Deems, J. S., Painter, T. H., & Finnegan, D. C. (2013). Lidar measurement of snow depth: A  
618 review. *Journal of Glaciology*, 59(215), 467–479. <https://doi.org/10.3189/2013JoG12J154>
- 619 Ellis, C. R., Pomeroy, J. W., & Link, T. E. (2013). Modeling increases in snowmelt yield and  
620 desynchronization resulting from forest gap-thinning treatments in a northern mountain  
621 headwater basin. *Water Resources Research*, 49(2), 936–949. <https://doi.org/10.1002/wrcr.20089>
- 623 Essery, R., Pomeroy, J. W., Parviainen, J., & Storck, P. (2003). Sublimation of snow from  
624 coniferous forests in a climate model. *Journal of Climate*, 16(11), 1855–1864. [https://doi.org/10.1175/1520-0442\(2003\)016%3C1855:SOSFCF%3E2.0.CO;2](https://doi.org/10.1175/1520-0442(2003)016%3C1855:SOSFCF%3E2.0.CO;2)
- 626 Floyd, W. C. (2012). *Snowmelt energy flux recovery during rain-on-snow in regenerating forests*  
627 (p. 180) [PhD Thesis, University of British Columbia]. <https://doi.org/https://dx.doi.org/10.14288/1.0073024>
- 629 Fryer, B. Y. G. I., Johnson, E. A., Fryer, G. I., & Johnson, E. A. (1988). Reconstructing  
630 Fire Behaviour and Effects in a Subalpine Forest. *The Journal of Applied Ecology*, 25(3),  
631 1063–1072. <https://doi.org/https://doi.org/10.2307/2403766>
- 632 Gelfan, A. N., Pomeroy, J. W., & Kuchment, L. S. (2004). Modeling forest cover influences on  
633 snow accumulation, sublimation, and melt. *Journal of Hydrometeorology*, 5(5), 785–803.  
634 [https://doi.org/10.1175/1525-7541\(2004\)005%3C0785:MFCIOS%3E2.0.CO;2](https://doi.org/10.1175/1525-7541(2004)005%3C0785:MFCIOS%3E2.0.CO;2)
- 635 Golding, D. L., & Swanson, R. H. (1978). Snow accumulation and melt in small forest openings  
636 in Alberta. *Canadian Journal of Forest Research*, 8(4), 380–388. <https://doi.org/https://doi.org/10.1139/x78-057>
- 638 Harder, P., & Pomeroy, J. W. (2013). Estimating precipitation phase using a psychrometric  
639 energy balance method. *Hydrological Processes*, 27(13), 1901–1914. <https://doi.org/https://doi.org/10.1002/hyp.9799>
- 641 Harder, P., Pomeroy, J. W., & Helgason, W. D. (2020). Improving sub-canopy snow depth  
642 mapping with unmanned aerial vehicles: Lidar versus structure-from-motion techniques.  
643 *Cryosphere*, 14(6), 1919–1935. <https://doi.org/10.5194/tc-14-1919-2020>
- 644 Harpold, A. A., Krogh, S. A., Kohler, M., Eckberg, D., Greenberg, J., Sterle, G., & Broxton,  
645 P. D. (2020). Increasing the efficacy of forest thinning for snow using high-resolution

- 646 modeling: A proof of concept in the Lake Tahoe Basin, California, USA. *Ecohydrology*,  
647 13(4). <https://doi.org/10.1002/eco.2203>
- 648 Hedstrom, N. R., & Pomeroy, J. W. (1998). Measurements and modelling of snow interception  
649 in the boreal forest. *Hydrological Processes*, 12(10-11), 1611–1625. [https://doi.org/10.1002/\(SICI\)1099-1085\(199808/09\)12:10/11%3C1611::AID-HYP684%3E3.0.CO;2-4](https://doi.org/10.1002/(SICI)1099-1085(199808/09)12:10/11%3C1611::AID-HYP684%3E3.0.CO;2-4)
- 650 Herwitz, S. R., & Slye, R. E. (1995). Three-dimensional modeling of canopy tree interception  
651 of wind-driven rainfall. *Journal of Hydrology*, 168(1-4), 205–226. [https://doi.org/10.1016/0022-1694\(94\)02643-P](https://doi.org/10.1016/0022-1694(94)02643-P)
- 652 Hijmans, R. J. (2024). *terra: Spatial Data Analysis*. <https://cran.r-project.org/package=terra>
- 653 Katsushima, T., Kato, A., Aiura, H., Nanko, K., Suzuki, S., Takeuchi, Y., & Murakami, S.  
654 (2023). Modelling of snow interception on a Japanese cedar canopy based on weighing  
655 tree experiment in a warm winter region. *Hydrological Processes*, 37(6), 1–16. <https://doi.org/10.1002/hyp.14922>
- 656 Kim, E., Gatebe, C., Hall, D., Newlin, J., Misakonis, A., Elder, K., Marshall, H. P., Hiem-  
657 stra, C., Brucker, L., De Marco, E., Crawford, C., Kang, D. H., & Entin, J. (2017).  
658 NASA’s snowex campaign: Observing seasonal snow in a forested environment. *2017  
659 IEEE International Geoscience and Remote Sensing Symposium (IGARSS)*, 1388–1390.  
660 <https://doi.org/10.1109/IGARSS.2017.8127222>
- 661 Kobayashi, D. (1987). Snow accumulation on a narrow board. *Cold Regions Science and  
662 Technology*, 13(3), 239–245. [https://doi.org/https://doi.org/10.1016/0165-232X\(87\)90005-X](https://doi.org/https://doi.org/10.1016/0165-232X(87)90005-X)
- 663 Kozak, A., & Kozak, R. A. (1995). Notes on regression through the origin. *Forestry Chronicle*,  
664 71(3), 326–330. <https://doi.org/https://doi.org/10.5558/tfc71326-3>
- 665 Langs, L. E., Petrone, R. M., & Pomeroy, J. W. (2020). A  $\delta^{18}\text{O}$  and  $\delta^2\text{H}$  stable water  
666 isotope analysis of subalpine forest water sources under seasonal and hydrological stress  
667 in the Canadian Rocky Mountains. *Hydrological Processes*, 34(26), 5642–5658. <https://doi.org/10.1002/hyp.13986>
- 668 LAStools. (2024). *Efficient LiDAR Processing Software (version 240220, academic)*. <http://rapidlasso.com/LAStools>

- 675 Lehtonen, I., Kämärainen, M., Gregow, H., Venäläinen, A., & Peltola, H. (2016). Heavy snow  
676 loads in Finnish forests respond regionally asymmetrically to projected climate change.  
677 *Natural Hazards and Earth System Sciences*, 16(10), 2259–2271. <https://doi.org/10.5194/nhess-16-2259-2016>
- 679 Lumbrazo, C., Bennett, A., Currier, W. R., Nijssen, B., & Lundquist, J. (2022). Evaluating  
680 Multiple Canopy-Snow Unloading Parameterizations in SUMMA With Time-Lapse  
681 Photography Characterized by Citizen Scientists. *Water Resources Research*, 58(6), 1–22.  
682 <https://doi.org/10.1029/2021WR030852>
- 683 Lundberg, A., & Hallidin, S. (1994). Evaporation of intercepted snow: Analysis of govern-  
684 ing factors. *Water Resources Research*, 30(9), 2587–2598. <https://doi.org/10.1029/94WR00873>
- 686 Lundquist, J. D., Dickerson-Lange, S., Gutmann, E., Jonas, T., Lumbrazo, C., & Reynolds, D.  
687 (2021). Snow interception modelling: Isolated observations have led to many land surface  
688 models lacking appropriate temperature sensitivities. *Hydrological Processes*, 35(7), 1–20.  
689 <https://doi.org/10.1002/hyp.14274>
- 690 MacDonald, J. P. J. (2010). *Unloading of intercepted snow in conifer forests* (Master of  
691 Science August, University of Saskatchewan; pp. 0–93). <http://hdl.handle.net/10388/etd-09302010-145706>
- 693 Mahat, V., & Tarboton, D. G. (2014). Representation of canopy snow interception, unloading  
694 and melt in a parsimonious snowmelt model. *Hydrological Processes*, 28(26), 6320–6336.  
695 <https://doi.org/10.1002/hyp.10116>
- 696 Moeser, D., Stähli, M., & Jonas, T. (2015). Improved snow interception modeling using  
697 canopy parameters derived from airborne LiDAR data. *Water Resources Research*, 51(7),  
698 5041–5059. <https://doi.org/https://doi.org/10.1002/2014WR016724>
- 699 Musselman, K. N., Pomeroy, J. W., & Link, T. E. (2015). Variability in shortwave irradiance  
700 caused by forest gaps: Measurements, modelling, and implications for snow energetics.  
701 *Agricultural and Forest Meteorology*, 207, 69–82. <https://doi.org/https://doi.org/10.1016/j.agrformet.2015.03.014>
- 703 Natural Resources Canada. (2024). *Precise point positioning*. <https://webapp.crsr-scrs.nrcan.ca/>

- 704 rncan.gc.ca/geod/tools-outils/ppp.php
- 705 Nock, C. A., Lecigne, B., Taugourdeau, O., Greene, D. F., Dauzat, J., Delagrange, S.,  
706 & Messier, C. (2016). Linking ice accretion and crown structure: towards a model  
707 of the effect of freezing rain on tree canopies. *Annals of Botany*, 117(7), 1163–1173.  
708 <https://doi.org/https://doi.org/10.1093/aob/mcw059>
- 709 Pfister, R., & Schneebeli, M. (1999). Snow accumulation on boards of different sizes and  
710 shapes. *Hydrological Processes*, 13(14-15), 2345–2355. [https://doi.org/https://doi.org/10.1002/\(SICI\)1099-1085\(199910\)13:14/15%3C2345::AID-HYP873%3E3.0.CO;2-N](https://doi.org/https://doi.org/10.1002/(SICI)1099-1085(199910)13:14/15%3C2345::AID-HYP873%3E3.0.CO;2-N)
- 711 Pomeroy, J. W., Brown, T., Fang, X., Shook, K. R., Pradhananga, D., Armstrong, R., Harder,  
712 P., Marsh, C., Costa, D., Krogh, S. A., Aubry-wake, C., Annand, H., Lawford, P., He,  
713 Z., Kompanizare, M., & Moreno, J. I. L. (2022). The cold regions hydrological modelling  
714 platform for hydrological diagnosis and prediction based on process understanding. *Journal  
715 of Hydrology*, 615(128711), 1–25. <https://doi.org/10.1016/j.jhydrol.2022.128711>
- 716 Pomeroy, J. W., Fang, X., & Ellis, C. R. (2012). Sensitivity of snowmelt hydrology in Marmot  
717 Creek, Alberta, to forest cover disturbance. *Hydrological Processes*, 26(12), 1891–1904.  
718 <https://doi.org/10.1002/hyp.9248>
- 719 Pomeroy, J. W., Marsh, P., & Gray, D. M. (1997). Application of a distributed blowing snow  
720 model to the arctic. *Hydrological Processes*, 11(11), 1451–1464. [https://doi.org/10.1002/\(SICI\)1099-1085\(199709\)11:11%3C1451::aid-hyp449%3E3.0.co;2-q](https://doi.org/10.1002/(SICI)1099-1085(199709)11:11%3C1451::aid-hyp449%3E3.0.co;2-q)
- 721 Pomeroy, J. W., Parviainen, J., Hedstrom, N., & Gray, D. M. (1998). Coupled modelling of  
722 forest snow interception and sublimation. *Hydrological Processes*, 12(15), 2317–2337. [https://doi.org/10.1002/\(SICI\)1099-1085\(199812\)12:15%3C2317::AID-HYP799%3E3.0.CO;2-X](https://doi.org/10.1002/(SICI)1099-1085(199812)12:15%3C2317::AID-HYP799%3E3.0.CO;2-X)
- 723 Pomeroy, J. W., & Schmidt, R. A. (1993). The Use of Fractal Geometry in Modelling Inter-  
724 cepted Snow Accumulation and Sublimation. *Eastern Snow Conference*, 50, 231–239.
- 725 R Core Team. (2024). *R: A Language and Environment for Statistical Computing*. R Foun-  
726 dation for Statistical Computing. <https://www.r-project.org/>
- 727 Rittger, K., Raleigh, M. S., Dozier, J., Hill, A. F., Lutz, J. A., & Painter, T. H. (2020). Canopy  
728 Adjustment and Improved Cloud Detection for Remotely Sensed Snow Cover Mapping.  
729 *Water Resources Research*, 56(6), n/a. <https://doi.org/10.1029/2019WR024914>

- 733 Roesch, A., Wild, M., Gilgen, H., & Ohmura, A. (2001). A new snow cover fraction parameterization for the ECHAM4 GCM. *Climate Dynamics*, 17(12), 933–946. <https://doi.org/10.1007/s003820100153>
- 734
- 735
- 736 Safa, H., Krogh, S. A., Greenberg, J., Kostadinov, T. S., & Harpold, A. A. (2021). Unraveling the Controls on Snow Disappearance in Montane Conifer Forests Using Multi-Site Lidar. *Water Resources Research*, 57(12), 1–20. <https://doi.org/10.1029/2020WR027522>
- 737
- 738
- 739 Satterlund, D. R., & Haupt, H. F. (1967). Snow catch by Conifer Crowns. *Water Resources Research*, 3(4), 1035–1039. <https://doi.org/https://doi.org/10.1029/WR003i004p01035>
- 740
- 741 Schmidt, R. A., & Pomeroy, J. W. (1990). Bending of a conifer branch at subfreezing temperatures: implications for snow interception. *Canadian Journal of Forest Research*, 20(8), 1251–1253. <https://doi.org/10.1139/x90-165>
- 742
- 743
- 744 Schmidt, R. A., & Troendle, C. A. (1989). Snowfall into a forest and clearing. *Journal of Hydrology*, 110(3-4), 335–348. [https://doi.org/10.1016/0022-1694\(89\)90196-0](https://doi.org/10.1016/0022-1694(89)90196-0)
- 745
- 746 Smith, C. D. (2007). Correcting the wind bias in snowfall measurements made with a Geonor T-200B precipitation gauge and alter wind shield. *87th AMS Annual Meeting*.
- 747
- 748 Staines, J., & Pomeroy, J. W. (2023). Influence of forest canopy structure and wind flow on patterns of sub-canopy snow accumulation in montane needleleaf forests. *Hydrological Processes*, 37(10), 1–19. <https://doi.org/10.1002/hyp.15005>
- 749
- 750
- 751 Storck, P., Lettenmaier, D. P., & Bolton, S. M. (2002). Measurement of snow interception and canopy effects on snow accumulation and melt in a mountainous maritime climate, Oregon, United States. *Water Resources Research*, 38(11), 1–16. <https://doi.org/10.1029/2002wr001281>
- 752
- 753
- 754
- 755 Troendle, C. A. (1983). The Potential for Water Yield Augmentation From Forest Management in the Rocky Mountain Region. *Journal of the American Water Resources Association*, 19(3), 359–373. <https://doi.org/10.1111/j.1752-1688.1983.tb04593.x>
- 756
- 757
- 758 Valante, F., David, J. S., & Gash, J. H. C. (1997). Modelling interception loss for two sparse eucalypt and pine forests in central Portugal using reformulated Rutter and Gash analytical models. *Journal of Hydrology*, 190(1-2), 141–162. [https://doi.org/10.1016/S0022-1694\(96\)03066-1](https://doi.org/10.1016/S0022-1694(96)03066-1)
- 759
- 760
- 761

- 762 Van Stan, J. T., Siegert, C. M., Levia, D. F., & Scheick, C. E. (2011). Effects of wind-  
763 driven rainfall on stemflow generation between codominant tree species with differing crown  
764 characteristics. *Agricultural and Forest Meteorology*, 151(9), 1277–1286. <https://doi.org/10.1016/j.agrformet.2011.05.008>
- 765
- 766 Varhola, A., Coops, N. C., Weiler, M., & Moore, R. D. (2010). Forest canopy effects on  
767 snow accumulation and ablation: An integrative review of empirical results. *Journal of*  
768 *Hydrology*, 392(3-4), 219–233. <https://doi.org/10.1016/j.jhydrol.2010.08.009>
- 769 Vionnet, V., Mortimer, C., Brady, M., Arnal, L., & Brown, R. (2021). Canadian historical  
770 Snow Water Equivalent dataset (CanSWE, 1928–2020). *Earth System Science Data*, 13(9),  
771 4603–4619. <https://doi.org/10.5194/essd-13-4603-2021>
- 772 Watanabe, S., & Ozeki, J. (1964). Study of fallen snow on forest trees (II). Experiment on the  
773 snow crown of the Japanese cedar. *Jap. Govt. Forest Exp. Sta. Bull*, 169, 121–140.
- 774 Wheeler, K. (1987). *Interception and redistribution of snow in a subalpine forest on a storm-*  
775 *by-storm basis*. Western Snow Conference. <http://sites/westernsnowconference.org/PDFs/1987Wheeler.pdf>
- 776

## 777 10 Supporting Information

### 778 10.1 Detailed Description of UAV-Lidar Methodology

779 The REIGL miniVUX-2 laser operates at a near infrared wavelength with a laser beam foot-  
780 print of 0.160 m x 0.05 mm (at 100 m above ground). The accuracy and precision of the  
781 miniVUX-2 is described by REIGL for a lab environment of 0.015 m and 0.01 m respectively  
782 (at 50 m above ground). The miniVUX-2 was configured with a laser pulse repetition rate of  
783 200 kHz, field of view of 360°, scan speed of 31.09 revolutions s<sup>-1</sup> and an angular step width  
784 of 0.0558°, resulting in an expected average point cloud density of 107 returns m<sup>-2</sup> for each  
785 flight path.

786 Georeferenced point clouds with x, y, and z coordinates for each laser return were generated

following methods outlined by Harder et al. (2020) and Staines & Pomeroy (2023) to reconcile survey lidar, IMU and GNSS data. A ground-based GNSS system was positioned on a permanent monument during each survey and underwent precise point positioning (PPP) correction by Natural Resources Canada (2024). Differential GNSS correction of the UAV trajectory was conducted using the ground-based PPP GNSS observations and the POSPac UAV software. The UAV-lidar point clouds were then transformed from a sensor referenced coordinate system to a georeferenced coordinate system (EPSG:32611 - WGS 84 / UTM zone 11N) using the RIEGL Riprocess Software. A vertical offset of up to 6 cm between UAV-lidar flight lines was observed in the resulting point clouds on March 13<sup>th</sup> and 14<sup>th</sup>, 2024 and was attributed to IMU position drift. This offset between flight lines was corrected using the BayesStripAlign software v2.24 (BayesMap Solutions, 2024), which reduces relative and absolute uncertainties in the vertical elevation of the point cloud using the ground control points (GCP) collected across the study site using a differential GNSS rover.

Quality control, ground classification and calculation of the change in between two UAV-lidar point clouds was conducted using the LAStools software package (LAStools, 2024). The ground classification was conducted using the “lasground\_new” function (LAStools, 2024) for both the pre and post snowfall event point clouds, with a step size set to 2 m and 8 substeps (ultra\_fine setting). The offset and spike options were set to remove points that are more than 0.1 m above or below the initial ground surface estimate surface which “lasground\_new” fits to the last returns. This function is based on an algorithm outlined by Axelsson (2000), describing the process of making the initial ground surface element.

The change in elevation between the two UAV-lidar surveys was interpreted as the increase in snow accumulation,  $\Delta HS$  over the snowfall event. This change was calculated using a point-to-grid subtraction method, using the “lasheight” function from the LAStools (2024) software, as in Deems et al. (2013) and Staines & Pomeroy (2023). The pre snowfall event point cloud from “lasground\_new” by “lasheight” to construct a “ground” TIN. Subsequently, the height of each post snowfall event point above the ground TIN, resulting in a point cloud representing  $\Delta HS$ . This point cloud was then converted into a raster of  $\Delta HS$  with a grid cell resolution

815 of  $5 \times 5$  cm using the “*las2dem*” function. Further quality control and resampling of the 5 cm  
 816 raster of  $\Delta HS$  was conducted using the ‘Terra’ R package (Hijmans, 2024). Areas that were  
 817 disturbed over the snowfall event during the in-situ snow survey and values that exceeded the  
 818 .999th quantile were removed. To help remove any remaining noise a 25 cm  $\Delta HS$  raster was  
 819 generated by computing the median of the 5 cm  $\Delta HS$  values within each 25 cm grid cell.  
 820 A comparison of UAV-liar and in-situ snow survey measurements over the March 13–14th  
 821 snowfall event and associated error metrics are shown in Figure 13.

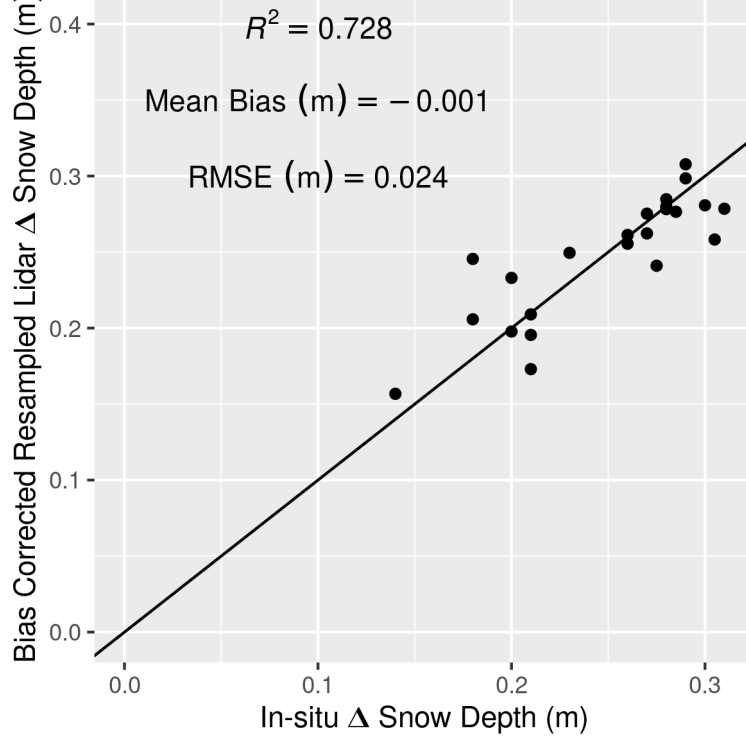


Figure 13: UAV-liar and in-situ snow survey measurements over the March 13–14th snowfall event and associated error metrics.

## 822 10.2 Linear Regression Models Through the Origin

823 Kozak & Kozak (1995) noted, the default  $R^2$  value provided for least squares models forced  
 824 through the origin by many statistical packages can be misleading. Therefore, these  $R^2$  values

were adjusted using Equation 10 in Kozak & Kozak (1995) and two statistical tests as described by Kozak & Kozak (1995) were used to verify whether a no-intercept model (forced through the origin) was appropriate for this data compared to a with-intercept model. The first test evaluated if the intercept of the with-intercept was significantly different from zero using p-value provided by the ‘summary’ function from the ‘stats’ package in R (R Core Team, 2024). The second test examined if there was a significant difference between the no-intercept and with-intercept models by testing if the residual sum of squares was different between the no-intercept and full model, assessed via Equation 15 in Kozak & Kozak (1995). If the first test indicated a significant difference, and the second did not, the no-intercept model could be deemed statistically justified (Kozak & Kozak, 1995).

### 10.3 Wind Speed Profile

The displacement height ( $d_0$ , m) and roughness length of momentum ( $z_0$ , m) were estimated over five events where the anemometers were known to be clean of snow. The mean wind speed of each event for the three different anemometers is shown in Figure 14.

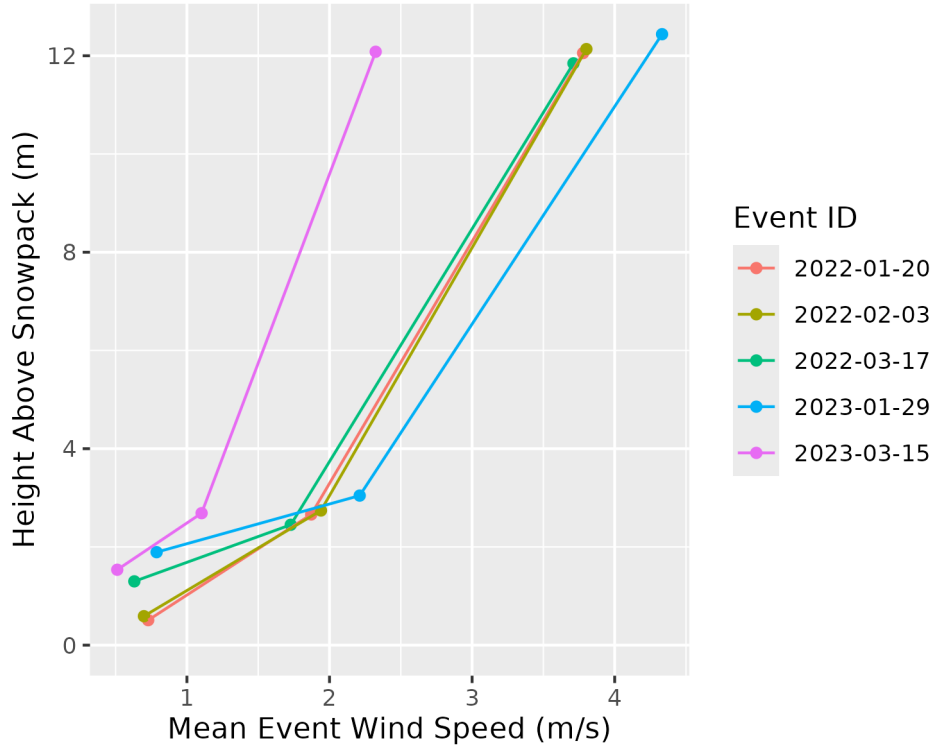


Figure 14: Wind profiles showing the average wind speed at differing heights above the surface snowpack. Wind speeds were averaged for three anemometers over five events when the anemometers were known to be clean of snow.